9-1-2024

Regiongrow3D: A Deterministic Analysis for Characterizing Discrete Three-Dimensional Landslide Source Areas on a Regional Scale

Nicolas W. Mathews
U.S. Geological Survey

Ben A. Leshchinsky
Oregon State University

Benjamin B. Mirus
U.S. Geological Survey

Michael J. Olsen
Oregon State University

Adam M. Booth
Portland State University

Citation Details

Mathews, N. W., Leshchinsky, B. A., Mirus, B. B., Olsen, M. J., & Booth, A. M. (2024). RegionGrow3D: A Deterministic Analysis for Characterizing Discrete Three-Dimensional Landslide Source Areas on a Regional Scale. Journal of Geophysical Research: Earth Surface, 129(9). Portico. https://doi.org/10.1029/2024jf007815

JGR Earth Surface

RESEARCH ARTICLE
10.1029/2024JF007815

RegionGrow3D: A Deterministic Analysis for Characterizing Discrete Three-Dimensional Landslide Source Areas on a Regional Scale

Nicolas W. Mathews[1,2], Ben A. Leshchinsky[3], Benjamin B. Mirus[1], Michael J. Olsen[2], and Adam M. Booth[4]

[1]U.S. Geological Survey, Geologic Hazards Science Center, Golden, CO, USA, [2]School of Civil and Construction Engineering, Oregon State University, Corvallis, OR, USA, [3]College of Forestry, Oregon State University, Corvallis, OR, USA, [4]Department of Geology, Portland State University, Portland, OR, USA

Key Points:

- RegionGrow3D is a regional-scale three-dimensional slope stability model that grows discrete landslide volumes to achieve force equilibrium
- RegionGrow3D is parameterized using a range of input parameters to quantify the size, location, and likelihood of landslide initiation
- Modeled landslides are used to quantify geomorphic scaling laws and rainfall thresholds that consider model input uncertainty

Supporting Information:

Supporting Information may be found in the online version of this article.

Correspondence to:

N. W. Mathews,
nmathews@usgs.gov

Citation:

Mathews, N. W., Leshchinsky, B. A., Mirus, B. B., Olsen, M. J., & Booth, A. M. (2024). RegionGrow3D: A deterministic analysis for characterizing discrete three-dimensional landslide source areas on a regional scale. *Journal of Geophysical Research: Earth Surface*, *129*, e2024JF007815. https://doi.org/10.1029/2024JF007815

Received 7 MAY 2024
Accepted 7 AUG 2024

Abstract Regional-scale characterization of shallow landslide hazards is important for reducing their destructive impact on society. These hazards are commonly characterized by (a) their location and likelihood using susceptibility maps, (b) landslide size and frequency using geomorphic scaling laws, and (c) the magnitude of disturbance required to cause landslides using initiation thresholds. Typically, this is accomplished through the use of inventories documenting the locations and triggering conditions of previous landslides. In the absence of comprehensive landslide inventories, physics-based slope stability models can be used to estimate landslide initiation potential and provide plausible distributions of landslide characteristics for a range of environmental and forcing conditions. However, these models are sometimes limited in their ability to capture key mechanisms tied to discrete three-dimensional (3D) landslide mechanics while possessing the computational efficiency required for broad-scale application. In this study, the RegionGrow3D (RG3D) model is developed to broadly simulate the area, volume, and location of landslides on a regional scale (≥1,000 km^2) using 3D, limit-equilibrium (LE)-based slope stability modeling. Furthermore, RG3D is incorporated into a susceptibility framework that quantifies landsliding uncertainty using a distribution of soil shear strengths and their associated probabilities, back-calculated from inventoried landslides using 3D LE-based landslide forensics. This framework is used to evaluate the influence of uncertainty tied to shear strength, rainfall scenarios, and antecedent soil moisture on potential landsliding and rainfall thresholds over a large region of the Oregon Coast Range, USA.

Plain Language Summary Landslides are potentially destructive natural hazards that may impact topography, ecology, and important infrastructure. Often, previously triggered landslides are used to better understand where landslides may occur in the future, but in some regions, previous landslides may be poorly documented or characterized. In lieu of these data, models capturing the physics tied to landsliding may be paired with digital topography to predict landslide potential across landscapes. However, existing models are limited in their ability to efficiently capture the realistic geometry of three-dimensional (3D) landslides across large landscapes. This study presents RegionGrow3D, a new model that identifies slope instabilities throughout large regions, and then grows those instabilities into landslides of previously unknown geometry by balancing forces within the underlying soil. The model is applied to a region in the Oregon Coast Range, USA to develop empirical relationships between landslide area, volume, and frequency for a range of rainfall scenarios and to determine the amount of rainfall required to trigger landslides on specific terrain features. Furthermore, because soil parameters are highly uncertain at this spatial scale (≥1,000 km^2), a 3D landslide model is used to forensically assess soil strength from previously documented landslides in the area.

1. Introduction

Shallow landslides cause loss and damage to life, property, and infrastructure on a global scale, and are exacerbated by high levels of soil moisture induced by rainfall (Terzaghi, 1950; Wieczorek, 1996). Regional-scale assessments of rainfall-induced shallow landslides often utilize event-based landslide inventories to determine: (a) where landslides may occur through susceptibility maps (Highland & Bobrowsky, 2008; Pourghasemi et al., 2018; Reichenbach et al., 2018), (b) the size and frequency of landslides through empirical scaling laws (Guzzetti et al., 2009; Malamud et al., 2004), and (c) the magnitude of trigger required to cause landsliding

Table 1
Summary of Regional-Scale, Limit Equilibrium Slope Stability Models

Model characteristics					Representative spatial scale		
Model name	References	Spatial dimensions	Discrete	Complex geometry[a]	Spatial scale (km^2)[b]	Pixel resolution (m)	References
Translational Landslides							
TRIGRS	Baum et al. (2010)	1D	N	N	>1000	10	Alvioli and Baum (2016)
SHALSTAB	Dietrich et al. (1995)	1D	N	N	<10	10	Dietrich et al. (1995)
TRIGRS w/Clustering[c]	Alvioli et al. (2014)	1D	Y	N	<10	10	Alvioli et al. (2014)
3DTLE	Hess et al. (2017)	3D	Y	N	100–1000	3–150	Hess et al. (2017)
STEP-TRAMM	Lehmann and Or (2012)	3D	Y	Y	10–100	10	Lehmann et al. (2019)
MD-STAB w/Spectral Clustering Search Algorithm	Bellugi, Milledge, Dietrich, McKean, et al. (2015)	3D	Y	Y	<10	2	Bellugi, Milledge, Dietrich, Perron, and McKean (2015)
RegionGrow3D	This study	3D	Y	Y	>1000	6	This study
Rotational Landslides							
r.rotstab	Mergili et al. (2014)	3D	Y	N	10–100	5	Mergili et al. (2014)
SCOOPS3D	Reid et al. (2015)	3D	Y	N	10–100	30	He et al. (2021)

[a]Complex geometry is defined as planform landslide geometry other than elliptical or rectangular. [b]Determined from a review of literature and may not represent the maximum applicable scale. [c]In this model, TRIGRS is used to identify unstable cells that are then grouped together by proximity.

through rainfall thresholds (Segoni et al., 2018). However, merging these hazard assessment techniques is challenging due to incompatibilities in the information used to develop them.

Many susceptibility maps estimate the likelihood and location of potential landslides using either probabilistic or deterministic methods (Highland & Bobrowsky, 2008; Reichenbach et al., 2018). Probabilistic methods compute landslide susceptibility using statistical relationships based on existing inventories of landslides, topography, and a variety of data layers (e.g., vegetation, climatic data; Lee, 2005; Lee & Talib, 2005; Highland & Bobrowsky, 2008; van Westen et al., 2008; Reichenbach et al., 2018). However, these approaches rely on sufficient inventory completeness and are only representative of the data used for model construction. Thus, they cannot be extrapolated to other regions or conditions (e.g., seismicity, rainfall, environmental conditions) for which there are insufficient data.

Regional-scale landslide susceptibility may also be evaluated using process-based, deterministic slope stability models that account for the physics tied to landslide initiation (e.g., Baum et al., 2010; Dietrich et al., 1995; Godt et al., 2008; Hess et al., 2017; Lu & Godt, 2008; Montgomery & Dietrich, 1994; Okimura & Ichikawa, 1985). In contrast to probabilistic approaches, incorporation of physics and process makes deterministic models less constrained to the bounds of observed landslide occurrence data, enabling simulation of a variety of hypothetical conditions, including rainfall (Baum et al., 2010; Brien & Reid, 2008; Godt et al., 2008; Lehmann et al., 2019; Montgomery & Dietrich, 1994) and seismicity (Hess et al., 2017; Zhang & Wang, 2019). When combined with hydromechanical models to compute transient changes in pore water pressure from rainfall infiltration, the stability of hillslopes subjected to rainfall may be determined on a regional scale (Baum et al., 2010; Godt et al., 2008). However, deterministic approaches must balance the complexity of slope stability models, uncertainties in model parameterization, and the spatial scale of their application. Thus, many regionally applied deterministic approaches utilize simple one-dimensional (1D) or two-dimensional (2D) slope stability models, such as the infinite slope or Culmann wedge (Bordoni et al., 2015; Lu & Godt, 2008; Medwedeff et al., 2020; Mirus et al., 2007; Perkins et al., 2017; Taylor, 1948; Terzaghi et al., 1996). These models, while applicable at large spatial scales and fine resolution, cannot capture the physics associated with discrete three-dimensional (3D) landslide geometry (Table 1).

Models that simulate 3D physics and discrete landsliding have been developed for regional assessments (Table 1). Using a 3D method of columns that considered unsaturated hydrological conditions, intercolumn root strength,

and discrete landslide failure, Lehmann and Or (2012) characterized the processes associated with the onset of shallow landslides. Milledge et al. (2014) used a 3D model to examine the controls on landslide size and shape based on soil depth and saturation ratio. Bellugi, Milledge, Dietrich, McKean, et al. (2015) combined the MD-STAB model (Milledge et al., 2014) with a spectral clustering search algorithm to model landslides with complex shapes diverging from elliptical or rectangular without assuming their geometry a priori. Mergili et al. (2014) considered deep-seated and shallow failures to produce a regional-scale assessment of landsliding in Italy. SCOOPS3D (Reid et al., 2015), which uses a 3D adaptation of Bishop's Simplified Method, has been used to assess the distribution of deep-seated landslides triggered by seismicity (Zhang & Wang, 2019). However, these models may not simultaneously (a) be applicable to scales beyond an individual hillslope or catchment (Table 1), (b) capture complex planform landslide geometry (Table 1), and (c) be parameterized to consider the heterogeneity of soil strength parameters at a regional scale.

Regional-scale landslide hazard assessment commonly relies on geomorphic scaling laws, such as relationships between landslide area, volume, and frequency (Guzzetti et al., 2009; Malamud et al., 2004; Tanyaş et al., 2019). Traditionally, these scaling laws are established through the statistical assessment of landslide inventories, some of which are tied to either one or more rainfall events (Gao et al., 2018; Guzzetti et al., 2012; Malamud et al., 2004; Patton et al., 2023). It is important that inventories are carefully prepared by skilled practitioners so that they are of sufficient quality for analysis. Physics-based models may supplement the data required to constrain these scaling relationships in lieu of a high-quality landslide inventory (e.g., Alvioli et al., 2014; Medwedeff et al., 2020). However, modeling studies of a sufficiently broad spatial scale to develop scaling relationships typically utilize 1D, grid-based analyses that do not consider 3D, discrete, and complex landslide geometries (Table 1). Further, 1D methods such as the infinite slope approach may underestimate landslide susceptibility in gentler terrain or entrainment of downslope landslide material due to its reliance on single-cell topographic parameters such as slope. A model that simulates the physics of discrete 3D landslides and the mobilization of downslope soils while remaining applicable on large spatial scales may better capture larger landslides with gentler slope angles than those typically predicted using 1D, grid-based slope stability analyses, and in turn, improve upon scaling relationships developed using physics-based models.

Rainfall thresholds define the amount of rainfall, typically in terms of intensity, I, and duration, D, required to cause the onset of slope instability (Baum & Godt, 2010; Caine, 1980; Guzzetti et al., 2007; Keefer et al., 1987). Most rainfall thresholds are created using landslide inventories, with some incorporating antecedent rainfall or soil moisture conditions within a temporal window of interest (Bogaard & Greco, 2018; Mirus, Becker et al., 2018; Mirus, Morphew, & Smith et al., 2018; Valenzuela et al., 2018). However, in the absence of both climatic and inventory data, some studies have implemented physics-based slope stability models to constrain regional-scale rainfall thresholds (e.g., De Vita et al., 2013; Fusco et al., 2021; Lehmann et al., 2019; Napolitano et al., 2016; Thomas et al., 2018; Zhang et al., 2020). Using the Transient Rainfall Infiltration and Grid-Based Regional Slope-Stability model (TRIGRS 2.0, Baum et al., 2010), which simulates transient rainfall infiltration using the linearized Richards' equation and computes slope stability for each pixel using the infinite slope method, Alvioli et al. (2014) developed intensity-duration (I-D) thresholds by applying infiltration of varying intensity and duration to a digital elevation model (DEM), where thresholds were defined as the intensity and duration that caused at least 10% of the grid cells to fail. Alvioli et al. (2014) also developed area-frequency relationships (e.g., Malamud et al., 2004); however, individual landslides were defined by clustering patches of unstable pixels assessed using the infinite slope method, as opposed to computing the equilibrium of discrete landslide volumes. Marin (2020) implemented the TRIGRS model using rasters of synthetic rainfall to compute I-D thresholds for each cell of a DEM. However, to our knowledge, no study has yet to model 3D, discrete landslides on a regional scale, use them to create rainfall thresholds, and relate those thresholds to geomorphic parameters, uncertainty of failure, or the spatial heterogeneity of variables associated with the onset of rainfall-induced landsliding. Doing so would enable consideration of diverse landslide characteristics associated with rainfall thresholds (i.e., mean landslide slope, likelihood of failure), supplementing traditional static and homogeneous I-D threshold approaches.

To more effectively model landslide initiation on scales broad enough to develop geomorphic scaling laws and rainfall thresholds, a 3D regional-scale slope stability approach that models complex and discrete landslide geometry, maintains computational efficiency, and is parameterized to capture uncertainty in heterogeneous soil properties is key. In this study, we present a computationally efficient, physics-based 3D landslide initiation model called *RegionGrow3D* (RG3D; Mathews & Leshchinsky, 2024). Using principles of 3D limit equilibrium (LE),

RG3D assesses the size and location of discrete landslide volumes on a regional scale by identifying localized instabilities within a DEM and then growing those instabilities by incorporating downslope columns of soil until force equilibrium is achieved. In this study, RG3D is parameterized with a hydromechanical model, remotely sensed antecedent soil moisture data, and spatial distributions of rainfall—tied to various storm recurrence intervals—to determine hydrologically derived stresses within the soil. Uncertainties in Mohr-Coulomb shear strength are considered by using a 3D stability analysis to forensically assess a suite of inventoried landslides (Bunn et al., 2020a, 2020b) and develop a probability distribution of soil strength. This distribution enables the evaluation of the likelihood of landslide initiation through an RG3D-based susceptibility framework.

Using susceptibility outputs, we assess the influence of shear strength uncertainty and various storm scenarios on (a) event-based landslide distributions for each month of the water year, (b) spatial distributions of landslide density, (c) rainfall thresholds related to geomorphic properties and parameter heterogeneity, and (d) landslide geomorphic scaling laws (e.g., area-frequency, area-volume) within the Oregon Coast Range, USA. We compare these results to geomorphic scaling laws from global inventories (Malamud et al., 2004) and inventories of rainfall-induced shallow landslides (Emberson et al., 2022; Martin et al., 2002).

2. RegionGrow3D Slope Stability Method

2.1. Three-Dimensional Limit Equilibrium

RG3D uses 1D LE to identify local instabilities on a regional scale and 3D LE to grow those instabilities into discrete 3D landslide polygons at incipient failure (Figures 1a and 1b). RG3D satisfies vertical and horizontal force equilibrium but does not consider moment equilibrium. First, the resultant normal intercolumn force, Q, is calculated for each column of soil in the DEM, where column dimensions are defined by the DEM cell size and an assumed slip surface depth (Figure 1f). Q is synonymous with the remainder of all horizontal forces for a given column. To better estimate forces stemming from realistic landslide geometry, Q is also evaluated within a boundary structure of soil surrounding each discrete landslide at each step of growth (Figure 1c). The process for applying RG3D is illustrated in the flowchart shown in Figure 2. RG3D requires a DEM with a corresponding estimate of soil depth for each pixel as well as estimates of soil shear strength and subsurface hydrological conditions. In this study, we estimate soil depth using a non-linear landscape evolution model (Roering, 2008), hydrological conditions using van Genuchten (1980) parameters and an unsaturated hydromechanical model, and soil strength using Mohr-Coulomb shear strength parameters, as determined using a 3D LE-based inversion method.

The resultant normal intercolumn force, in the direction of sliding, is derived from the equation for horizontal equilibrium:

$$Q = N \sin\beta - \left[c'A + (N - uA)\tan\phi'\right]\cos\beta \tag{1}$$

where c' is effective cohesion, A is the column basal slip surface area, u is porewater pressure (when u is positive) or suction stress (when u is negative) at the base of the column, and ϕ' is the effective angle of internal friction. Porewater pressure and suction are computed using a hydromechanical model discussed later in this paper. The normal force on the slip surface, N, is derived from the equation of vertical equilibrium:

$$N = \frac{W + uA\tan\phi'\sin\beta - c'A\sin\beta}{\cos\beta + \tan\phi'\sin\beta} \tag{2}$$

β is the resultant slip surface angle:

$$\beta = \tan^{-1}\left(\sqrt{\left(\frac{dz}{dx}\right)^2_{\text{slip}} + \left(\frac{dz}{dy}\right)^2_{\text{slip}}}\right) \tag{3}$$

where $\left(\frac{dz}{dx}\right)_{\text{slip}}$ and $\left(\frac{dz}{dy}\right)_{\text{slip}}$ are the elevation gradients of the slip surface in the X and Y directions (easting and northing), dx and dy are the cell dimensions in the X and Y directions, and dz represents the vertical change in

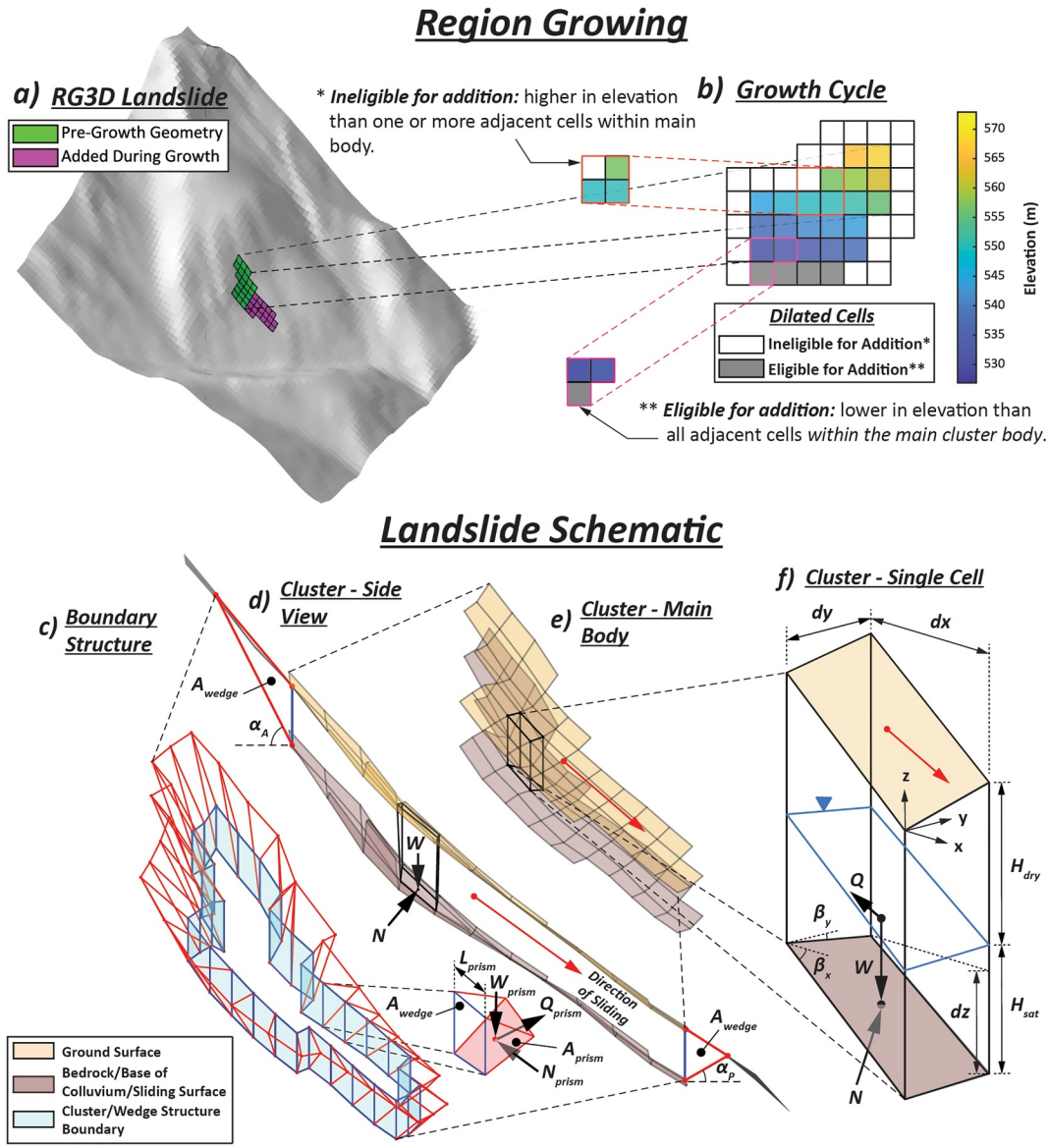

Figure 1. (a) Pre- and post-growth landslide geometry and (b) dilated columns for a single growth cycle. The selected small clusters within the orange and pink polygons highlight a single dilated cell and the adjacent cells within the main cluster that its elevation is compared to in order to determine eligibility for addition; (c) boundary structure and schematic of a single boundary prism; (d) side view of landslide cluster; (e) overview of landslide cluster; and (f) free body diagram of a single column.

elevation of the slip surface in each lateral direction. We assume that all failures occur in regolith or colluvium above bedrock, hereafter simply referred to as soil, and that slip surfaces exist at the base of each soil column. Slip surface angles in the X and Y directions are computed as follows:

$$\beta_x = \tan^{-1}\left(\left(\frac{dz}{dx}\right)_{\text{slip}}\right) \tag{4}$$

$$\beta_y = \tan^{-1}\left(\left(\frac{dz}{dy}\right)_{\text{slip}}\right) \tag{5}$$

Soil weight, W, is defined as

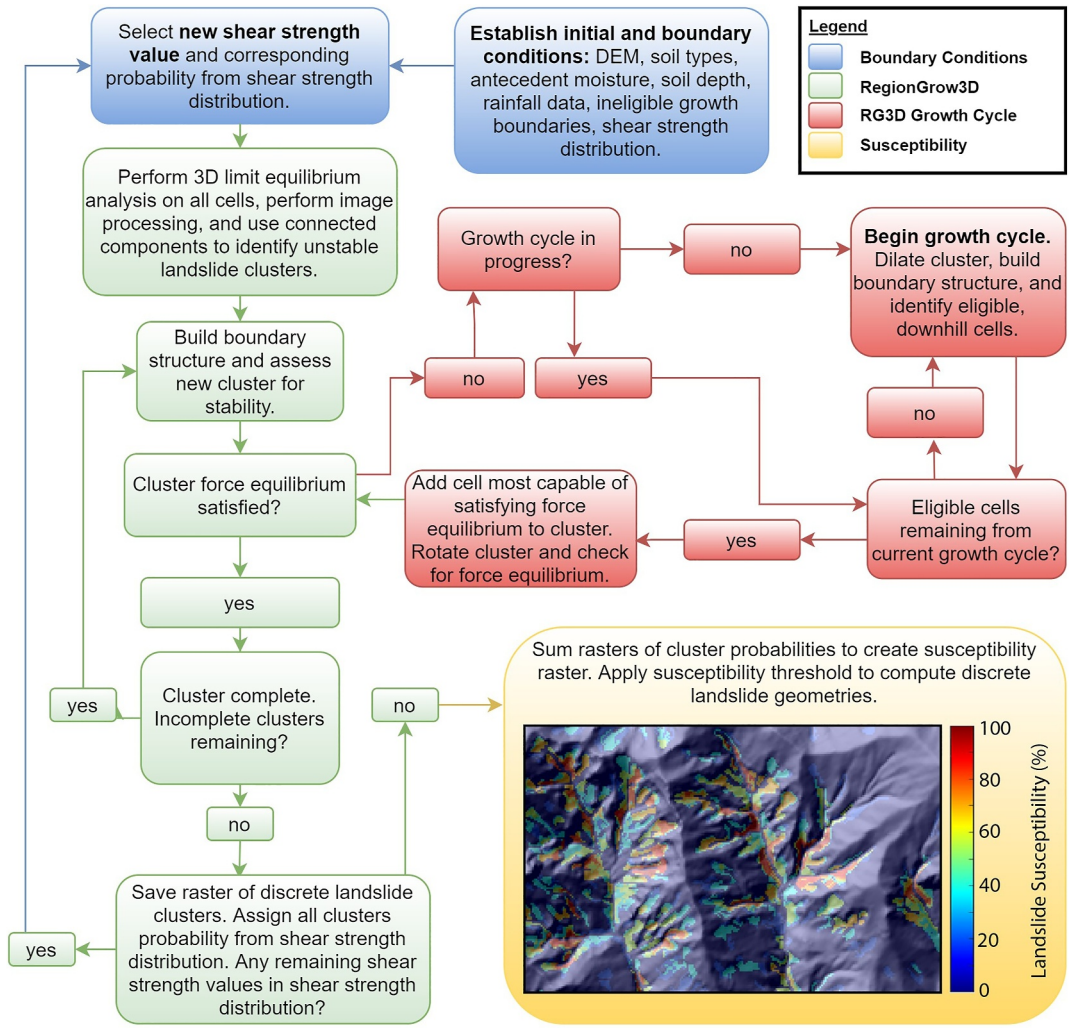

Figure 2. Flowchart illustrating the creation of boundary and initial conditions, the RegionGrow3D slope stability model, model parameterization, and the susceptibility framework. Hillshade was created using lidar provided by the Oregon Lidar Consortium (https://www.oregon.gov/dogami/lidar/pages/index.aspx).

$$W = dxdy\left(H_{\text{dry}}\gamma_{\text{dry}} + H_{\text{sat}}\gamma_{\text{sat}}\right) \tag{6}$$

where H_{dry} and H_{sat} are the soil thickness of dry and saturated soil, and γ_{dry} and γ_{sat} are the unit weight of dry and saturated soil. For calculating soil unit weight, we assume the unsaturated zone is composed of completely dry soil and the saturated zone is composed of fully wetted soil and combine these weights accordingly (Equation 6), but when determining suction stress, we use the variable soil-water content profile as described later in Section 4.4. Unit weights are computed for each soil textural classification using volumetric water content and specific gravity, G_s (Evans & Baker, 2021):

$$\gamma_{\text{dry}} = \left[G_s(1-\theta_s) + \theta_r\right]\gamma_w \tag{7}$$

$$\gamma_{\text{sat}} = \left[G_s(1-\theta_s) + \theta_s\right]\gamma_w \tag{8}$$

where θ_s is saturated volumetric water content, θ_r is residual water content, and γ_w is the unit weight of water. Due to differences in soil structure, θ_s and θ_r vary for each soil texture, as defined using a lookup table based on the ROSETTA pedotransfer model (Schaap et al., 2001). We assume that G_s is 2.65 for all soil textures, although it

may be defined as any value within this framework. Column base slip surface area, A, is computed using the Hovland (1977) approach:

$$A = dxdy\frac{\left(1-\sin^2\beta_x\,\sin^2\beta_y\right)^{\frac{1}{2}}}{\cos\beta_x\cos\beta_y} \tag{9}$$

The normal, intercolumn resultant force is resolved into X and Y components, Q_x and Q_y:

$$Q_x = \frac{\tan\beta_x}{\sqrt{\tan^2\beta_x+\tan^2\beta_y}}Q \tag{10}$$

$$Q_y = \frac{\tan\beta_y}{\sqrt{\tan^2\beta_x+\tan^2\beta_y}}Q \tag{11}$$

Slope stability is then assessed for each column, where $Q \le 0$ indicates stability and $Q > 0$ indicates instability. An image processing technique called *connected components* is implemented in MATLAB to identify groups of interconnected unstable columns (8-pixel connectivity); each group of unstable columns is considered an individual landslide initiation cluster. Unstable columns that overlay the *ineligible growth boundary* raster (e.g., a topographic ridgeline), discussed in a later section, are excluded from any initiation clusters. For computational stability during cluster growth, single unstable columns are made stable. Also, spurs of unstable columns that are one cell wide and several cells long are made stable, and single stable columns surrounded by unstable columns are made unstable. This is meant to eliminate instabilities that may be caused by noise in the high-resolution digital elevation data used in this study. Once all landslide initiation clusters have been identified using a 1D balance of forces, a boundary structure of soil is constructed around each cluster, and each cluster is subjected to a region growing process until it has achieved stability, or when the sum of forces has an absolute value less than an acceptable tolerance (Figure 2).

2.2. Landslide Boundary Forces

Following cluster creation and at the beginning of each growth cycle, a 3D structure of boundary soil, hereafter referred to as a *boundary structure*, is computed for each cluster to estimate forces stemming from realistic landslide geometry. This structure is composed of 2D wedges built around the perimeter of the landslide, which are connected to form a series of triangular prisms around the cluster main body (Figure 1c). The dip angle of the wedge oriented in the direction of sliding is defined by the passive wedge angle, α_P, providing a stabilizing buttress at the toe of the landslide, and the dip angle of the wedge opposite the orientation of the direction of sliding is defined by the active wedge angle, α_A (Rankine, 1857; Figure 1d):

$$\alpha_P = 45° - \frac{\phi'}{2} \tag{12}$$

$$\alpha_A = 45° + \frac{\phi'}{2} \tag{13}$$

In between these angles, the dip angle of each wedge, α_{wedge}, is defined using linear interpolation for the entire perimeter of the landslide:

$$\alpha_{\text{wedge}}(\omega) = \frac{(\omega-\omega_1)(\alpha_2-\alpha_1)}{\omega_2-\omega_1}+\alpha_1 \tag{14}$$

$$\begin{cases} \omega_1 = 0°; \omega_2 = 180°;\ \alpha_1 = \alpha_A;\ \alpha_2 = \alpha_P, & 0° \le \omega < 180° \\ \omega_1 = 180°; \omega_2 = 360°;\ \alpha_1 = \alpha_P;\ \alpha_2 = \alpha_A, & 180° \le \omega < 360° \end{cases} \tag{15}$$

where ω is the orientation angle in relation to the direction of sliding (ω equals 0° or 360° in the direction of sliding and 180° in the direction opposite of sliding). The direction of sliding, DOS (red arrow in Figures 1d–1f),

is the four-quadrant inverse tangent of force balances in the X and Y directions within the cluster main body (not including boundary structure forces):

$$\mathrm{DOS} = \tan^{-1}\left(\frac{\sum_{i=1}^{n} Q_{y_i}}{\sum_{i=1}^{n} Q_{x_i}}\right) \tag{16}$$

where i is the index of a given column and n is the total number of columns within the cluster main body. The inside depth of each boundary wedge is equal to the depth of the adjacent column within the cluster main body, and the outer edge of each wedge exits at the ground surface (Figure 1d). Once the geometry of each 2D wedge is defined, they are connected to form a series of 3D prisms around the main cluster body. Normal intercolumn forces are then computed for each prism, assuming that the downward facing plane is the slip surface (shaded light red in Figure 1c):

$$Q_{\mathrm{prism}} = N_{\mathrm{prism}} \sin \beta_{\mathrm{prism}} - \left[c' A_{\mathrm{prism}} + (N_{\mathrm{prism}} - u_{\mathrm{prism}} A_{\mathrm{prism}}) \tan \phi'\right] \cos \beta_{\mathrm{prism}} \tag{17}$$

$$Q_{x,\mathrm{prism}} = \frac{\tan \beta_{x,\mathrm{prism}}}{\sqrt{\tan^2 \beta_{x,\mathrm{prism}} + \tan^2 \beta_{y,\mathrm{prism}}}} Q_{\mathrm{prism}} \tag{18}$$

$$Q_{y,\mathrm{prism}} = \frac{\tan \beta_{y,\mathrm{prism}}}{\sqrt{\tan^2 \beta_{x,\mathrm{prism}} + \tan^2 \beta_{y,\mathrm{prism}}}} Q_{\mathrm{prism}} \tag{19}$$

where Q_{prism} is the prism normal intercolumn force, $Q_{x,\mathrm{prism}}$ and $Q_{y,\mathrm{prism}}$ are the X and Y components of the prism normal intercolumn force, β_{prism} is the resultant slip surface angle of the prism, $\beta_{x,\mathrm{prism}}$ and $\beta_{y,\mathrm{prism}}$ are the slip surface angles of the prism in the X and Y directions, A_{prism} is the area of the prism slip surface as computed using the Hovland (1977) approach, and u_{prism} is porewater pressure (when u_{prism} is positive) or suction stress (when u_{prism} is negative) at the prism slip surface. Because the slip surface of the prism spans in elevation from the ground surface to the bottom of the prism, we assume that u_{prism} is the mean value of u in between the ground surface and the depth of soil at the prism base. Values of u are computed for multiple depths and averaged using the hydromechanical model. W_{prism} is the weight of the prism:

$$W_{\mathrm{prism}} = V_{\mathrm{prism}} \times \gamma_{\mathrm{prism}} \tag{20}$$

where V_{prism} is the volume of the prism and γ_{prism} is the soil unit weight within the prism. For all prisms in the boundary structure, γ_{prism} is assumed to be equal to the mean unit weight of the entire cluster main body:

$$\gamma_{\mathrm{prism}} = \frac{W_{cl}}{V_{cl}} \tag{21}$$

where W_{cl} is the weight of the entire cluster main body and V_{cl} is the volume of the entire cluster main body. V_{prism} is computed as:

$$V_{\mathrm{prism}} = \frac{1}{2}(A_{\mathrm{wedge}}(\omega) + A_{\mathrm{wedge}}(\omega + d\omega)) \times L_{\mathrm{prism}} \tag{22}$$

where A_{wedge} is the area of a 2D wedge, $d\omega$ is the angle between two wedges, and L_{prism} is the length of a triangular prism or the distance between two adjacent wedges on the boundary of the cluster main body. Like the soil columns within the main cluster, the normal force acting on the prism slip surface is derived using the equation for vertical equilibrium:

$$N_{\text{prism}} = \frac{W_{\text{prism}} + u_{\text{prism}} A_{\text{prism}} \tan \phi' \sin \beta_{\text{prism}} - c' A_{\text{prism}} \sin \beta_{\text{prism}}}{\cos \beta_{\text{prism}} + \tan \phi' \sin \beta_{\text{prism}}} \tag{23}$$

2.3. Stability of Landslide Clusters

Once the intercolumn forces of each prism are computed, they are summed with those from the cluster main body:

$$Q_{cl,x} = \sum_{i=1}^{n} Q_{x_i} + \sum_{j=1}^{m} Q_{x,\text{prism}_j} \tag{24}$$

$$Q_{cl,y} = \sum_{i=1}^{n} Q_{y_i} + \sum_{j=1}^{m} Q_{y,\text{prism}_j} \tag{25}$$

$$Q_{cl} = \sqrt{{Q_{cl,x}}^2 + {Q_{cl,y}}^2} \tag{26}$$

where $Q_{cl,x}$ and $Q_{cl,y}$ are the summations of intercolumn forces for a given cluster in the X and Y directions, Q_{cl} is the resultant summation of intercolumn forces, j is the index of a given prism within the boundary structure, and m is the total number of prisms within the boundary structure. Stability for a given landslide cluster is determined as follows:

$$\begin{cases} \text{stable}, & |Q_{cl}| \leq E_{\text{allowable}} \\ \text{unstable}, & |Q_{cl}| > E_{\text{allowable}} \end{cases} \tag{27}$$

where $E_{\text{allowable}}$ is a force tolerance defining the threshold for closure, a typical component of LE slope stability techniques. In this study, $E_{\text{allowable}}$ is equal to 1% of the cluster total soil weight (including the weight of the boundary structure). To account for uncertainty in the cluster's direction of sliding, all forces within the landslide cluster are rotated 20° (clockwise) and −20° (counterclockwise) around the vertical axis, and stability is assessed for all orientations within this range. If force equilibrium is satisfied at any orientation, the landslide cluster is considered stable and ineligible for region growth (Figure 2). While this feature increases the likelihood of fulfilling force closure, it may also reduce the likelihood of capturing the full extent of unstable terrain. To balance these tradeoffs, RG3D may be parameterized with any angle to define the range of uncertainty tied to the direction of sliding. If force equilibrium is not satisfied, the cluster is considered unstable and region growing begins, a process in which downslope columns of potentially unstable soil are added to the cluster, typically increasing the net resisting force until force equilibrium is satisfied (Figure 2).

2.4. Convergence of Equilibrium Through Region Growing

For unstable clusters, downslope columns of soil are iteratively added to the cluster main body to both achieve force equilibrium and estimate realistic landslide geometry. Because columns are mobilized by an excess of driving force in the downslope direction at incipient failure and subsequent compression of downslope soil, only downslope columns are considered for additions. Although retrogression or post-initiation head scarp failure may occur, this is a complex and time-dependent mechanism not explicitly considered in this study. However, sensitivity studies considering both upslope growth and a simple head scarp failure mechanism are included in Supporting Information S1 (Text S1.1 and S1.2). As columns are added, the cluster typically grows into less steep terrain where soil is deeper, disproportionately adding resisting forces to the toe of the landslide until force equilibrium is satisfied. Further, as columns containing deeper soil are added to the toe of the landslide, prisms within the boundary structure may become deeper and more voluminous at the toe, buttressing the landslide and further contributing to resisting forces. Landslide cluster growth terminates if there are no remaining downslope columns to add or if the cluster grows into an ineligible growth boundary, even if force equilibrium has not yet been satisfied.

Region growing is performed for all unstable clusters and occurs in a series of *growth cycles* in which the main cluster body is first dilated by one column on all sides. Of these dilated cells, only those (a) downslope of all

adjacent columns within the main cluster body (i.e., only cells within the main body that touch the dilated cell in question, including those diagonally connected) and (b) not intersecting with an ineligible growth boundary or the DEM boundary are deemed eligible for addition to the cluster; the rest are discarded (Figure 1b). Eligible columns are then sorted by their ability to satisfy force equilibrium by, first, evaluating their resultant intercolumn force, $Q_{e,k}$, and the X and Y components of $Q_{e,k}$, Q_{e,x_k} and Q_{e,y_k}, where k is the index of a given column (Equations 1, 10, and 11). The capability of each eligible column to satisfy force equilibrium is defined as the difference between the sum of forces in the cluster and $Q_{e,k}$:

$$Q_{diff_k} = Q_{cl} - Q_{e,k} \tag{28}$$

where Q_{diff_k} is the force difference for column k. The column with the minimum value of Q_{diff} is deemed the most capable of satisfying the force equilibrium, added to the main cluster body, and removed from the list of eligible columns. Q_{cl} is then reassessed, the remaining eligible columns are re-sorted, and the most eligible column is again added to the cluster. This process repeats until the current growth cycle is complete or until force equilibrium is achieved. If force equilibrium is not achieved during the current growth cycle, the cluster is again dilated and another growth cycle begins (Figure 2). Each cluster is eroded by one column on all sides prior to the first growth cycle to ensure that a potentially stable landslide geometry smaller than the initial cluster is not missed. However, much of this eroded terrain is still incorporated by the boundary structure, and eroded columns at the toe are typically reincorporated during downslope growth. Also, for computational efficiency, a boundary structure is only built at the beginning of each growth cycle, as opposed to after each single column addition.

Typically, near the beginning of region growth, the most eligible column is that with the highest value of $Q_{e,k}$. However, near the end, columns with a lower value of $Q_{e,k}$ may be the most eligible, as a high $Q_{e,k}$ may exceed the requisite forces for most accurately satisfying force equilibrium. Although the completion of a given growth cycle may not induce force equilibrium, subsequent construction of boundary structure forces may be sufficient to induce cluster stability, in which case, the region growing process is considered complete. Q_{cl} is saved after each column addition during a growth cycle so that if any eligible columns stabilize the cluster beyond the threshold of error (i.e., "over-stabilizes" the cluster), they may be removed after the growth cycle. This enables post-growth assessment of the most stable cluster configuration. Once the most stable configuration of the landslide cluster is determined for a given growth cycle, that configuration is saved and the growth cycle is considered complete. Note that this approach is not aimed at finding the least stable (i.e., "critical") landslide geometry but rather all unstable cells that may compose a landslide. However, RG3D may be parameterized to assess critical failure geometry for rainfall-induced landslides (Section 7.1). It is also possible for multiple landslides to grow in proximity to each other and sometimes make contact. In this case, we assume that each cluster is an individual landslide for computational expedience. However, these landslides may be connected in post-processing for comparison to landslide inventories, which may struggle to make the distinction between two discrete landslides in contact.

3. Landslide Forensics and Susceptibility

Similar to other physics-based regional-scale slope stability models (Table 1), applying RG3D on a landscape for a single value of Mohr-Coulomb frictional strength, ϕ', produces discrete landslide shapes and addresses a binary question: *For a given set of input parameters, will a slope fail or not?* Some of the advantages of RG3D over previous approaches, including its computational efficiency (8.6 s per 1,000 landslides; section Text S2 in Supporting Information S1), facilitate probabilistic assessment of landslide susceptibility using iterative model runs with a wide range of possible input parameterizations. To characterize landslide susceptibility, or the size, location, and likelihood of landsliding, we implemented RG3D repeatedly within a susceptibility framework to (a) reflect the potential distribution of soil shear strengths observed throughout a landscape, and (b) assign probabilities to values of ϕ' to assess the likelihood of landsliding. To compute the distribution of ϕ', we back analyzed inventoried landslides using a landslide forensics framework based on reconstructed landslide failure geometries and 3D limit equilibrium (Bunn et al., 2020a, 2020b). This distribution is an input for the RG3D-based susceptibility framework, which enables assessment of landslide size, location, and probability for a range of rainfall scenarios. Antecedent soil moisture and rainfall are included in back analyses through incorporation of the hydromechanical model described in Section 4.4.

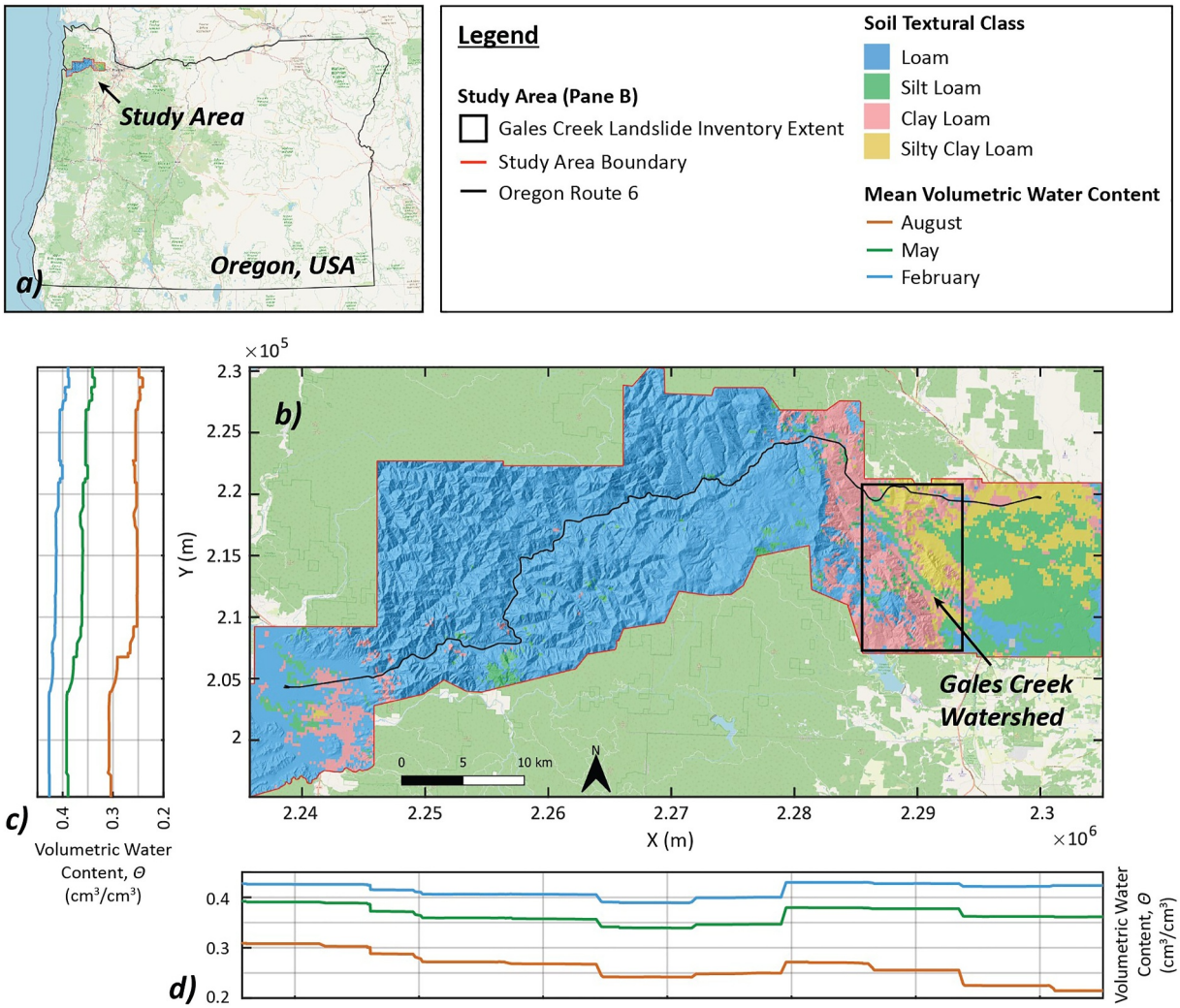

Figure 3. (a) Overview of the study area. Basemap provided by OpenStreetMap (OpenStreetMap contributors, 2017); (b) Map of study area and Gales Creek landslide inventory extent (landslide polygons shown in Figure S12 in Supporting Information S1). Hillshade was created using lidar provided by the Oregon Lidar Consortium (https://www.oregon.gov/dogami/lidar/pages/index.aspx). Highway network data provided by the Oregon Department of Transportation (Oregon Department of Transportation, 2017). Soil texture was determined using sand and clay content data from SoilGrids250m (Hengl et al., 2017). Distributions of mean θ for select months (February—blue, May—green, August—orange) for each (c) row and (d) column. Volumetric water content data is from SMAP (Reichle et al., 2019).

3.1. Estimating Three-Dimensional Rupture Surface Geometry

Back analysis of an inventoried landslide requires an estimate of its failure surface geometry. We estimate 3D rupture surface geometry by projecting a thin-plate spline beneath the inventoried landslide using angles derived from Rankine earth pressure theory (Bunn et al., 2020a; Rankine, 1857). The resulting spline provides a smooth failure surface constrained to a group of control points while still retaining realistic curvature. We applied this method to 696 landslides located in the Gales Creek watershed (Figure 3; Burns et al., 2012; Franczyk et al., 2019).

In section Text S3 in Supporting Information S1, we compare the size, slope angle, and canopy cover of these landslides to those predicted by RG3D and show that the inventoried landslides are typically larger in area, volume, and mean depth. This indicates that many of the inventoried landslides may be deep-seated and not representative of the shallow landslides we aim to assess using RG3D. However, to prevent inclusion of deep-seated landslides, only shallow landslides (mean thickness between 1 and 5 m)—as identified using the methods in Bunn et al. (2020a)—and those with a mean slope angle greater than, or equal to, 20° were forensically analyzed for shear strength (98 landslides in total; Figure S12 in Supporting Information S1).

3.2. Back-Calculation of Shear Strength Parameters

Using estimates of failure surface geometry and a 3D LE-based approach, we achieve force equilibrium by iteratively solving for ϕ' at the failure interface of each inventoried landslide, providing an estimate of shear strength for each one (Bunn et al., 2020b). Although cohesion may be considered, we assume that all soil strength is attributed to friction and that c' equals zero, which is reasonable considering the frictional nature of shallow soil landslides (Alberti et al., 2022). Apparent cohesion stemming from suction stress in partially saturated soil is considered. Reinforcement from tree roots can be an important factor in shallow landsliding (e.g., Cohen et al., 2011; Schmidt et al., 2001; Schwarz et al., 2010), but capturing the pullout mechanics of roots is complex and we do not consider it in this study. However, Text S1.4 in Supporting Information S1 quantifies the sensitivity of RG3D outputs to root cohesion. Triggering conditions for many of the landslides in the inventory are unknown; therefore, we assume typical "winter" antecedent soil moisture for initial groundwater conditions, estimated by averaging rasters of remotely sensed volumetric water content, θ, for 15 February from 2016 to 2019. We source 9-km-resolution rasters of θ from the Soil Moisture Active Passive (SMAP) satellite mission and resample them (nearest neighbor approach) to match the resolution of the DEM (6 m). The data used in this study are Level 4 (L4) soil moisture products, which are geophysical model outputs created using SMAP data collected via an orbiting radiometer (Reichle et al., 2019). We assume that inventoried landslides were caused by rainfall and apply a distribution of event rainfall corresponding to a 100-year recurrence interval. The Oregon Coast Range experiences subduction zone earthquakes, which are known to trigger landslides (Serey et al., 2019; Wartman et al., 2013). However, earthquakes have been shown to be a less prominent trigger of deep-seated landslides in the Oregon Coast Range when compared to rainfall (LaHusen et al., 2020) and we assume that the signatures of most shallow landslides occurring during the last known major earthquake (1700 AD; Goldfinger et al., 2012) have been erased through erosional processes (LaHusen et al., 2020). Thus, we do not consider inertial loading from seismicity during back analysis.

3.3. Landslide Susceptibility and Susceptibility-Based Discrete Landslide Failures

We create landslide susceptibility maps by considering multiple values of ϕ' and their respective probabilities as inputs for RG3D (Figure 2). Susceptibility maps expand upon RG3D outputs, which characterize binary failure conditions (e.g., *did the hillslope fail or not?*) by conveying the spatial distribution of landslide probability (i.e., *what is the likelihood of failure?*). We compute susceptibility as follows: (a) A probability distribution of ϕ' is computed via forensic back analysis (Figure S20 in Supporting Information S1); (b) RG3D is applied to the DEM for each bin of the distribution using its average value of ϕ'; (c) for a given bin, each landslide cluster is assigned that bin's corresponding probability. This process is repeated for the entire distribution of ϕ' with all other inputs held constant (e.g., antecedent soil moisture, rainfall, soil depth, boundary conditions, DEM), yielding a raster of landslide probability for each bin. Finally, these rasters are summed to create a susceptibility map that conveys the size, location, and the probability of landslide activity (example in Figure S17 in Supporting Information S1).

To compute binary metrics commonly used to assess landslide distributions (e.g., landslide density, area-volume relationships, magnitude-frequency relationships, rainfall thresholds), we create a map of discrete landslides by applying a selected threshold of susceptibility, T, to a susceptibility map. All pixels whose susceptibility is greater than or equal to T are clustered together using the *connected components* tool in MATLAB while those less than T are discarded. The result is a distribution of landslides that is based on the physics of discrete 3D landsliding, and may consider any probability of failure. These maps enable statistical analyses of landslide volume, area, mean slope, and other metrics for a variety of hypothetical rainfall conditions. Further, these amalgamated landslide shapes better capture what may be found in a landslide inventory, as post-event inventories may struggle to distinguish two shallow landslides in contact with each other.

4. Computation of Regional-Scale Inputs and Boundary Conditions

4.1. Ineligible Growth Boundaries

Without appropriate boundary conditions, landslide clusters may unrealistically wrap around ridgelines or grow across valley floors. We limit these behaviors using a raster of ineligible growth boundaries, which makes any superimposing columns stable, regardless of force balance, and ineligible for cluster addition during region growth (example shown in Figure S18 in Supporting Information S1). This raster is a combined network of

ridgelines and valley floors, where ridgelines constrain landslide cluster growth to singular hillslopes and valley floors prevent clusters from crossing drainages. Ridgelines are identified by first inverting the DEM:

$$Z_{\text{inv}} = -(Z - Z_{\text{max}}) + Z_{\text{min}} \tag{29}$$

where Z_{inv} is the inverted raster cell elevation, Z is the raster cell elevation, Z_{max} is the maximum raster elevation, and Z_{min} is the minimum raster elevation. Drainage flow accumulation is then computed using the *flowacc* function in MATLAB from TopoToolbox 2 (Schwanghart & Scherler, 2014). Drainages equal to, or exceeding, a user defined threshold of flow accumulation are identified as valleys within the inverted DEM, which become ridgelines when inverted back to original DEM elevations (parameterization discussed in Text S5 in Supporting Information S1). Valleys are identified using the same procedure but on the original DEM. The ridgeline and valley networks are then combined, and small remaining gaps are connected using image processing tools in MATLAB (Text S5 in Supporting Information S1).

4.2. Soil Depth

We assume that the slip surface for a given column exists at the base of the soil layer. In lieu of soil depth measurements, we estimate soil depth using a nonlinear slope-dependent model that simulates tectonic uplift, soil production, and erosion for a steady-state landscape over a given timespan (Roering, 2008). We assume an initial soil depth of 1 m, a timespan of 5,000 years, and parameterize the model to represent the Oregon Coast Range (Text S6 in Supporting Information S1). Although we assume a slip surface at the depth of soil for this study, RG3D may be parameterized with any slip surface geometry defined a priori.

4.3. Soil Textural Classification

The hydromechanical model relies on soil-water characteristics that vary between soil textural classifications. We assign soils a code representing one of 12 textural classes (Soil Survey Staff, 1975) using estimates of sand, clay, and silt content determined using machine learning and remotely sensed environmental covariates (SoilGrids250m; Hengl et al., 2017). We then assign van Genuchten (1980) parameters to each column in the DEM, based on soil texture, using a lookup table based on the ROSETTA pedotransfer model (Schaap et al., 2001). The spatial distribution of these parameters plays a crucial role in determining how effective stress evolves throughout the study area when subjected to varying degrees of antecedent soil moisture and rainfall.

4.4. Hydromechanical Model

Using a hydromechanical model and estimates of soil texture, antecedent soil moisture, and event rainfall, we compute a subsurface profile of θ which is used to derive effective stress and soil shear strength. We solve for subsurface water content by iteratively fitting a profile of θ to a remotely sensed value of θ at any given depth (Lehmann et al., 2019; Leshchinsky et al., 2021):

$$\theta(z) = \frac{\int_0^H \theta_r + (\theta_s - \theta_r)\left[1 + (\alpha h(z))^n\right]^{\left(-\left(1-\frac{1}{n}\right)\right)} dz}{H} \tag{30}$$

where α and n are van Genuchten fitting parameters, dz is depth increment integrated from the surface to a depth H, and h is head. We use values of θ from SMAP at 1-m deep to represent a reasonable depth of failure for shallow landslides. The resulting profile yields θ at any depth and enables determination of the saturated depth of soil, or where $\theta = \theta_s$. This depth is also where H_{dry} and H_{sat} are delineated for the computation of soil weight (Equation 6). Pore pressure (suction or positive), u, at any depth, z, is:

$$u(z) = -\gamma_w(-h_{\text{sat}} - z)\left[1 + \alpha((-h_{\text{sat}} - z)^n)\right]^{-(1-1/n)} \tag{31}$$

where h_{sat} is saturated pressure head. We introduce infiltration by considering an average volumetric water content, $\overline{\theta_o}$, and applying a rainfall intensity flux, I, for each timestep dt. We compute a new average water content profile, $\overline{\theta}$, for each time step:

$$\overline{\theta}(t,z) = \overline{\theta}(t - dt,z) + d\theta = \overline{\theta}(t - dt,z) + \frac{Idt}{H} \quad (32)$$

where t is time, and $d\theta$ is change in θ. We then compute a new profile of θ and u using Equations 30 and 31. After rainfall is applied, we convert the final profile into a lookup table for computational efficiency, later used to determine u for a given combination of soil depth, event rainfall intensity, and initial volumetric water content. A lookup table was created for all soil textural classifications. This simplified model accounts for both changes in pore water pressure—positive and negative—and groundwater table rise but is limited in that (a) infiltration is added instantaneously, (b) only vertical infiltration is considered (no lateral subsurface flow), and (c) all rainfall is considered infiltration (infiltration-excess runoff is not considered). However, RG3D could be parameterized with a model considering these components through a similar implementation of lookup tables.

5. Study Area and Regional-Scale Inputs

We apply RG3D to a 1,068-km^2 study area in the Oregon Coast Range that exhibits frequent landslide activity and contains a throughway, Oregon Highway 6, connecting the Willamette Valley to the Oregon Coast, from Washington County to Tillamook, Oregon (Figure 3). This region of the Oregon Coast Range features well-constrained climatic conditions, availability of high-resolution topographic data, and a high-quality landslide inventory for forensic evaluation. Geology varies throughout the study area, with the western region composed of marine sedimentary rocks, basalts, and a region of alluvial deposits west of the coastal mountains. The central region is mainly composed of basalts (Eocene-age Tillamook Volcanics, late Tertiary-age Columbia River Basalt), marine sedimentary rocks (Eocene-age Yamhill Formation), and diabase (diabase of Lee's Falls). The eastern region contains similar rock types as the central region and a large, relatively flat region of Missoula flood deposits east of the coastal mountains. The southwest region contains pockets of the landslide-prone early Tertiary Tyee Formation (rhythmically bedded sedimentary rocks; Franczyk et al., 2020; Smith & Roe, 2015). Surficial soil texture also varies with most of the west and central regions containing loam, with pockets of silt loam and clay loam throughout. The eastern region is composed of a mix of silt loam, silty clay loam, clay loam, and loam (Figure 3). Although surficial soils may not always represent soil texture at depth, this distribution provides a first-order estimate of soil parameters, which are used to compute hydrological response. Modeled soil depth tends to be deeper in valley bottoms (areas of high deposition) and shallower upon ridgelines or escarpments (areas of relatively high erosion rates; Text S7 in Supporting Information S1). Some deposits outside of the coastal mountains, namely the Missoula flood deposits east of the Gales Creek watershed (Figure 3), may be considerably deeper than those modeled in this study (Peterson et al., 2011). However, these deposits are characteristically flat and typically have negligible inventoried landslide activity (Franczyk et al., 2019) and RG3D-derived susceptibility values.

We source topographic light detection and ranging (lidar) data (0.91-m × 0.91-m bare-earth lidar) from the Oregon Lidar Consortium (https://www.oregon.gov/dogami/lidar/pages/index.aspx) and landslide inventory data (2D polygons from the Gales Creek watershed) from the Statewide Landslide Information Database for Oregon (SLIDO)—Release 4.0 (Figure 3; Burns et al., 2012; Franczyk et al., 2019; https://www.oregongeology.org/slido/), both provided by the Oregon Department of Geology and Mineral Industries (DOGAMI). We resampled lidar data to 6-m resolution and reproject the DEM to Oregon State Plane North (EPSG: 32126) prior to analysis. A map of landslide polygons is shown in Figure S12 in Supporting Information S1.

We compute spatial distributions of θ representing mean antecedent moisture conditions for each month of the year by averaging time histories of SMAP-based θ at 1-m depth (3-hr temporal resolution) spanning from 31 March 2015 to 28 August 2020 (methods are detailed in Text S8 in Supporting Information S1; example distributions for February, May, and August are shown in Figure 3). This approach provides a first-order approximation of mean antecedent moisture but does carry limitations. The 9-km grids of θ from SMAP may overlay various soil textures with different values of θ_s and θ_r, potentially mischaracterizing relative levels of soil saturation. SMAP may also be a worse predictor of landsliding than in situ measurements in some cases (Reichle et al., 2017; Thomas et al., 2019) but remains a valuable tool for estimating broad-scale seasonal changes in soil moisture across large landscapes as they relate to landslides (Bessette-Kirton et al., 2019). To account for inconsistencies between SMAP and in situ measurements, we reduced all SMAP-derived values of θ by a correction factor of 0.055 m^3/m^3 (Reichle et al., 2017). The hydrological parameterization of RG3D could be improved by

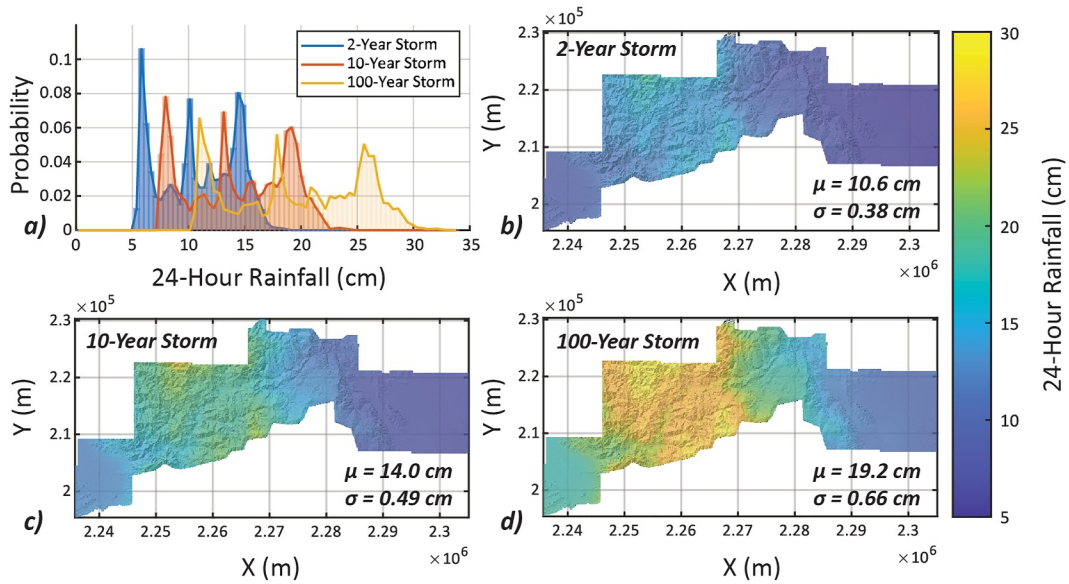

Figure 4. Distributions of 24-hr rainfall with mean values of rainfall, μ, and standard deviation, σ: (a) histograms of spatial rainfall distributions; (b) spatial patterns of rainfall for a 2-year storm; (c) 10-year storm; and (d) 100-year storm. Hillshade was created using lidar provided by the Oregon Lidar Consortium (https://www.oregon.gov/dogami/lidar/pages/index.aspx). Rainfall distributions are from the Oregon Department of Transportation Hydraulics Design Manual (Oregon Department of Transportation, 2014).

downscaling SMAP-derived θ distributions to better consider topographic convergence and to eliminate sharp gradients in θ at SMAP grid boundaries (e.g., Felsberg et al., 2021; Grieco et al., 2018). We source values of 24-hr event rainfall (I in Equation 32) for a range of recurrence intervals from the Oregon Department of Transportation (ODOT) hydraulics manual (ODOT, 2014; Figure 4).

We forensically computed a probability distribution of ϕ' using inventoried landslides for use within the susceptibility framework (Figure S20 in Supporting Information S1; Bunn et al., 2020a, 2020b), where lidar-mapped landslide deposits and head scarps (termed "scarp flanks in the SLIDO inventory") were used as inputs for failure geometry reconstruction (Figure S12 in Supporting Information S1). We assume that, in some cases, inventoried landslide deposits may overlap with the landslide failure surface; this is addressed within the forensics framework as described in Text S3 in Supporting Information S1. In total, we assessed 696 inventoried landslides within the Gales Creek watershed (Figure 3), but to best represent shallow landslides in the inventory, we only included 98 landslides with a mean depth of 1–5 m and a mean slope greater than 20° in the ϕ' distribution. Although we only consider frictional strength in this study, an analysis highlighting the sensitivity of RG3D outputs to mineral cohesion is discussed in Text S1.5 in Supporting Information S1.

6. Comparison to Landslide Inventory and Scaling Laws

6.1. Comparison to Landslide Inventory

We validate RG3D landslides against the Gales Creek inventory using receiver operating characteristic (ROC) curves and the associated area under the curve (AUC), which allows us to quantify true positive and false positive rates. For validation, we only generated RG3D landslides within a bounding box defined by the extents of the inventory and validated them against two versions of the inventory: (a) all landslides within the inventory ($n = 696$; purple in Figure S12 in Supporting Information S1) and (b) only those with a mean depth of 1–5 m and an average slope exceeding 20° ($n = 98$; green in Figure S12 in Supporting Information S1). Although the failure mechanisms are largely unknown for this inventory, version 2 is meant to best capture shallow landslides in soil. We assume average February antecedent conditions with a range of event rainfall recurrence intervals and use susceptibility thresholds ranging from 0% to 100% as cutoffs for ROC curve calculations.

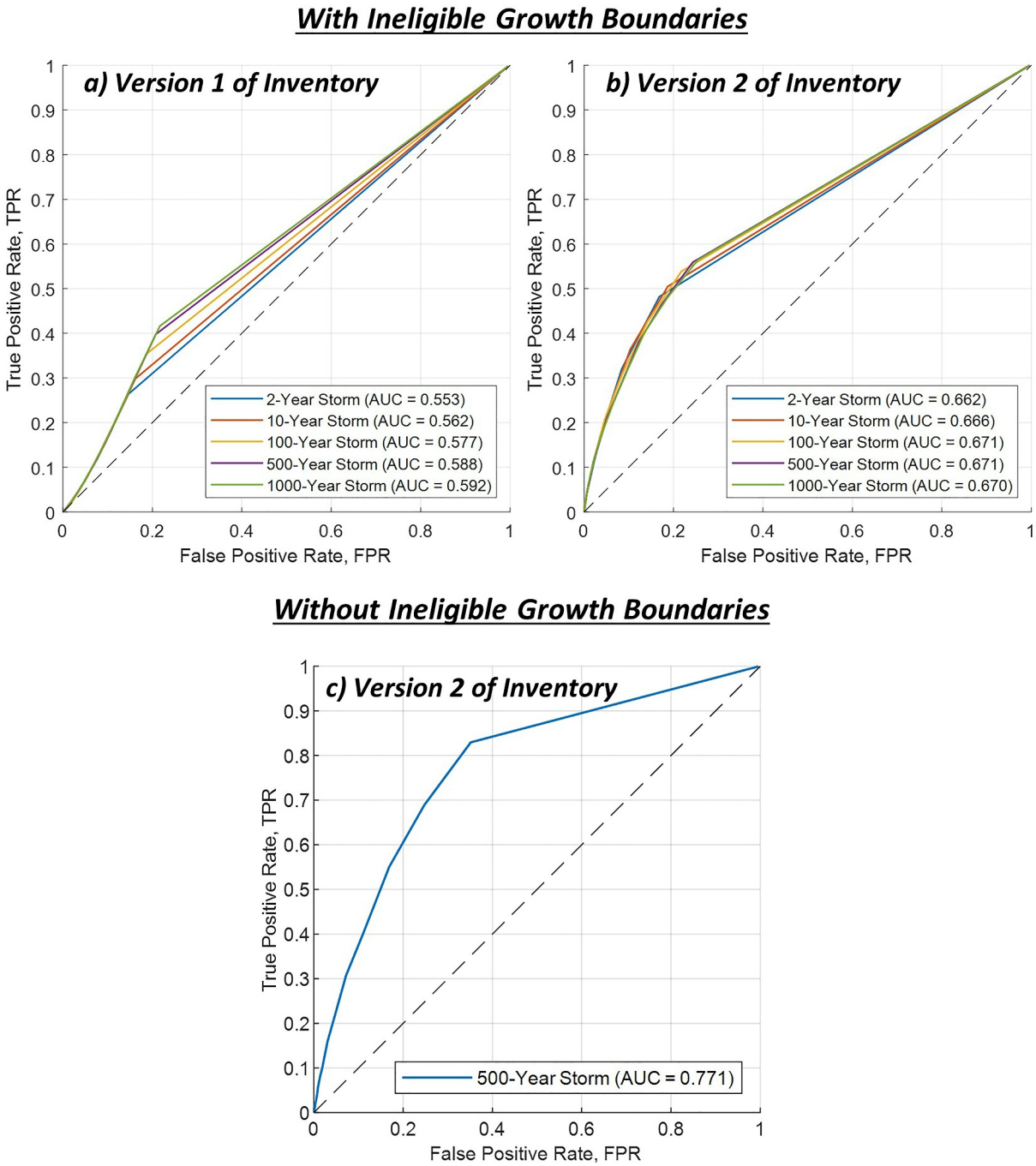

Figure 5. Receiver operating characteristic (ROC) curves and area under the curve (AUC) comparing RegionGrow3D landslides to the Gales Creek inventory: (a) version 1 with ineligible growth boundaries; (b) version 2 with ineligible growth boundaries; and (c) version 2 without ineligible growth boundaries.

AUC values are 0.55–0.59 for version 1 of the inventory, increasing with rainfall recurrence interval (i.e., rainfall intensity; Figure 5a), and 0.66–0.67 for version 2 (Figure 5b). Higher AUC indicates better model performance, indicating that the model performs best for higher rainfall intensities and when compared to shallow landslides only. However, this is reflective of a specific inventory and model parameterization, and would likely change for regions with different environmental conditions. Because RG3D landslides are generally smaller in area than those from the Gales Creek inventory (Text S3 in Supporting Information S1), we also compare RG3D landslides produced with ineligible growth boundaries disabled; this reduces restrictions on landslide growth, allowing them to grow larger during region growth. Comparing these data to version 2 and assuming a rainfall recurrence

interval of 500 years, which produced the highest AUC in previous comparisons, yields an AUC of 0.77 (Figure 5c). For context, 0.5 equates model performance to random guessing and 1.0 indicates perfect discrimination. Hosmer and Lemeshow (1989) classify 0.7 as the lower bound for "acceptable discrimination" and 0.8–0.9 as "excellent discrimination." Further details on the methods, assumptions, limitations, and results for this assessment are discussed in Text S3 in Supporting Information S1.

6.2. Geomorphic Scaling Relationships

We use discrete landslides derived from RG3D-based susceptibility maps to produce area-volume and area-frequency relationships for shallow landslides. We compute area-volume relationships using a power-law function:

$$V_L = \varepsilon \times A_L^{\alpha} \tag{33}$$

where V_L is the landslide volume, A_L is the landslide area, and ε and α are fitting parameters. Area and volume data are log-transformed and fit using a robust linear regression to reduce the influence of outliers (Guzzetti et al., 2009). We compare area-volume relationships developed using RG3D ($T = 50\%$) to an inventory of shallow landslides in British Columbia, Canada (Martin et al., 2002) representing a similar failure mechanism (shallow, translational) and climate (Pacific Northwest, USA). Because Martin et al. (2002) amalgamated landslide inventories tied to different rainfall events, we assumed mean antecedent moisture for February and develop area-volume relationships for a range of event rainfall recurrence intervals (Figure 6c). RG3D-based relationships show reasonable agreement with Martin et al. (2002) and all have an α value close to 1, indicating that soil depth is close to 1 m for most landslides and that landslide volume increases nearly linearly with area. This is heavily influenced by the soil depth model and would likely change with different parameterizations of slip surface depth.

We also compare RG3D landslides (mean February moisture, $T = 50\%$) to frequency-density (FD) and probability-density (PD) relationships from literature for a range of event rainfall recurrence intervals (Figures 6a and 6b). RG3D-based relationships contain similar scaling to those based on inventories (Malamud et al., 2004) and a "rollover" at the transition from larger to smaller landslides, a characteristic feature of area-frequency relationships (Malamud et al., 2004; Tanyaş et al., 2019). RG3D-based FD increases for higher magnitude rainfall events, similar to published FD relationships for a range of landslide-event magnitudes, m_L, tied to both rainfall and seismic triggers (Figure 6a; Malamud et al., 2004). RG3D-based PD shows agreement with Malamud et al. (2004) with a better fit for mid-sized landslides than very small and very large landslides where components of PD relationships are still a subject of debate, potentially influenced by censoring, physical and topographical controls, and other factors (Figure 6b; Tanyaş et al., 2019). Areas of poor fit likely stem from discrepancies in landslide type, as Malamud et al. (2004) included inventories with a range of failure styles and mechanisms (e.g., translational/rotational, shallow/deep, rainfall/earthquake) where we only considered translational, rainfall-induced shallow landslides. The uptick in FD and PD for very small landslides is likely caused by small failures predicted by RG3D and would likely be sensitive to changes in DEM resolution. Similar behavior has been observed in distributions of real landslides, for which PD at small areas is also sensitive to the spatial resolution of data used to create the landslide inventory (Malamud et al., 2004). Distributions may also be slightly influenced by the elimination of single-column and spur-like landslides. RG3D-based FD and PD distributions are also compared to a suite of shallow landslide inventories (Emberson et al., 2022) in Text S10 in Supporting Information S1. Overall, these comparisons indicate that model performance is reasonable and may be used in landscape scale experiments to interpret known geomorphic scaling laws.

7. Applications of Model

7.1. Transient Rainfall and Critical Failure Geometry

In contrast to classical limit equilibrium analyses, which aim to capture the most critical failure geometry for a given slope, RG3D is meant to capture the full extent of failure-prone material (i.e., any terrain associated with a factor of safety less than unity). However, there is relevance in finding critical geometry, or what is most likely to fail under a set of assumed conditions. In this case, the most critical terrain is that which fails during the wetting up process approaching our total amount of rainfall. To simulate the wetting up process, we ran RG3D iteratively for 2-cm increments of event rainfall, assuming February antecedent moisture conditions, 20 cm of total rainfall, and

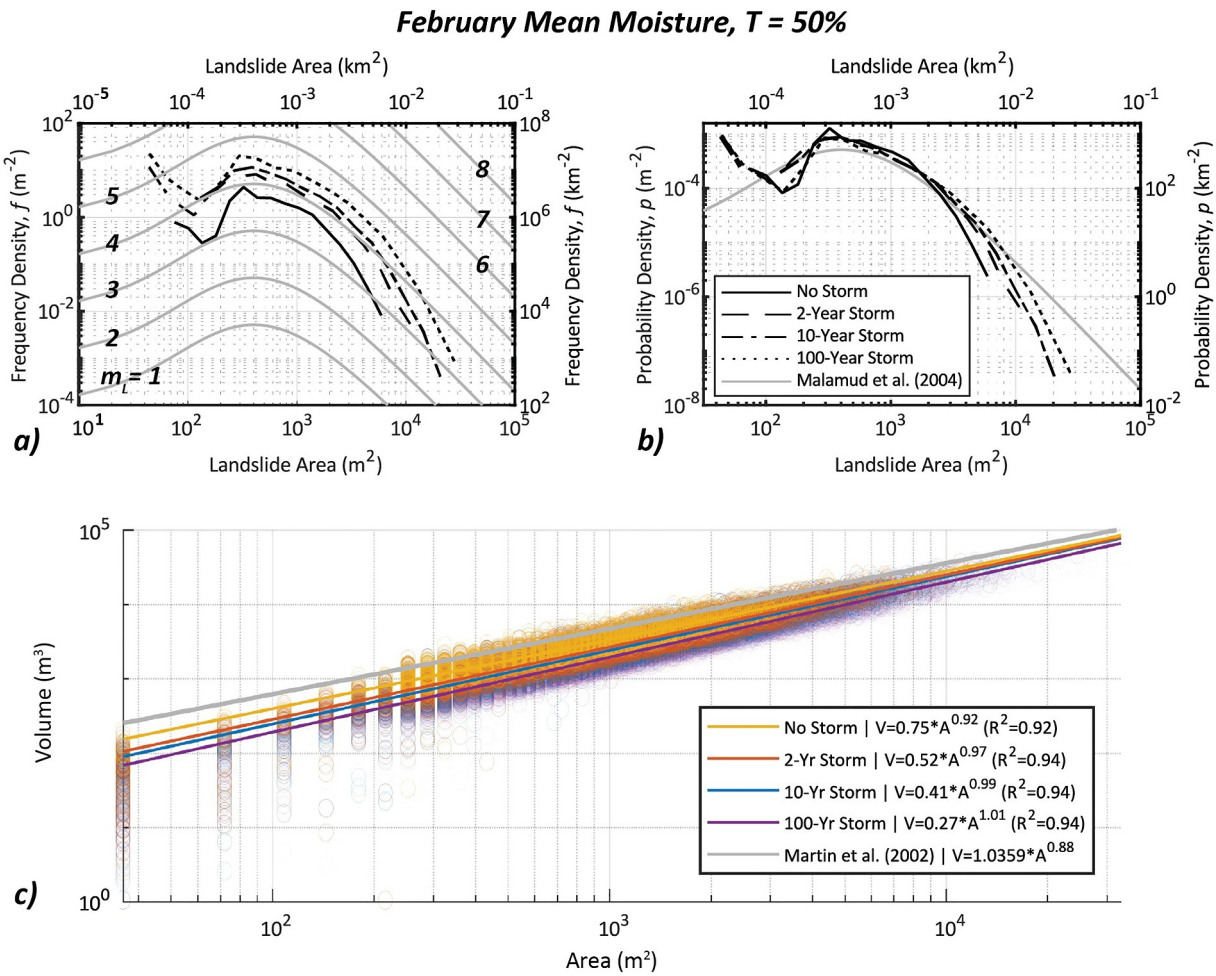

Figure 6. Comparison of geomorphic scaling relationships for February mean antecedent moisture and a range of event rainfall recurrence intervals: (a) frequency density of landslide areas; (b) probability density of landslide areas; (c) area-volume relationships. $\boldsymbol{T}$ = threshold of susceptibility. $\boldsymbol{V}$ = landslide volume. $\boldsymbol{A}$ = landslide area. $\boldsymbol{R^2}$ = coefficient of determination.

three friction angles. For the incremental application of rainfall, we performed a stability analysis for each 2-cm of cumulative rainfall (e.g., 0 cm, 2 cm, 4 cm…). Unstable terrain was deleted from the landscape after each RG3D stability assessment, making that terrain ineligible for failure in subsequent assessments (i.e., terrain that fails at 2 cm of cumulative rainfall cannot fail again at 4 cm of cumulative rainfall). Terrain that failed at lower cumulative rainfall was considered more critical than terrain that failed at higher cumulative rainfall. For comparison, we also applied 2, 8, 14, and 20 cm of rainfall prior to a single RG3D stability assessment for each friction angle, hereafter referred to as the "all-at-once" approach.

Failed volume is similar between the incremental approach and the all-at-once approach for up to 8 cm of cumulative rainfall, but diverges as rainfall increases (Figure 7a). For 20 cm of rainfall, the all-at-once approach produces higher amounts of failed volume than the incremental approach for all friction angles, with percent differences ranging from 11.0% to 13.1% (Table 2). This analysis quantifies the error associated with applying all rainfall before a stability assessment, as opposed to simulating the wetting up process, which requires additional computational expense. However, the computational efficiency of RG3D enables the assessment of temporal patterns of incipient landsliding using iterative analyses, providing insight into which terrain features may fail early in the wetting up process (Figure 7b; Figure S7 in Supporting Information S1).

For the incremental approach, we assume that failed material is deleted from the landscape instead of redistributed as a landslide deposit. This has implications for slope stability, as redistributed soil may alter the effective stress

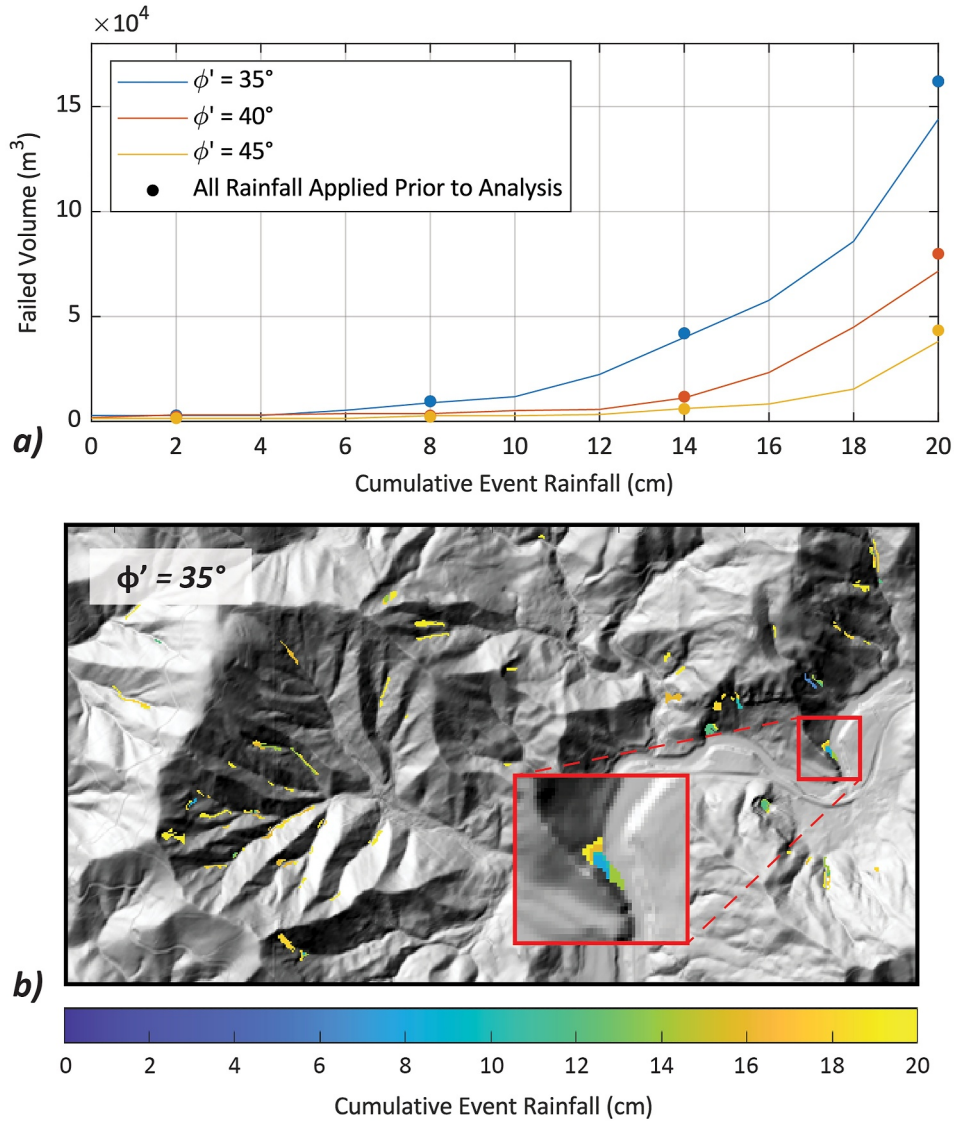

Figure 7. (a) Cumulative rainfall versus failed volume for selected friction angles, ϕ'. Curves represent cumulative failed volume as calculated using RegionGrow3D after each incremental 2-cm addition of rainfall. Points represent failed volume when the corresponding cumulative rainfall is added all-at-once prior to a RegionGrow3D slope stability assessment; (b) Map of landslides as computed using the incremental rainfall approach ($\phi' = 35°$). Lower values of cumulative rainfall represent terrain that failed earlier in the wetting up process. Additional maps for $\phi' = 40°$ and $\phi' = 45°$ are shown in Figure S7 in Supporting Information S1. Hillshade was created using lidar provided by the Oregon Lidar Consortium (https://www.oregon.gov/dogami/lidar/pages/index.aspx).

Table 2
Comparison of Failed Volumes for Incremental and "All-At-Once" Application of Rainfall

Friction angle, ϕ' (°)	Event rainfall applied (cm)	Failed volume (m^3; rainfall applied incrementally)	Failed volume (m^3; all rainfall applied prior to analysis)	Percent difference in failed volume
35	20	143,981	161,760	11.6%
40		71,585	79,885	11.0%
45		38,122	43,447	13.1%

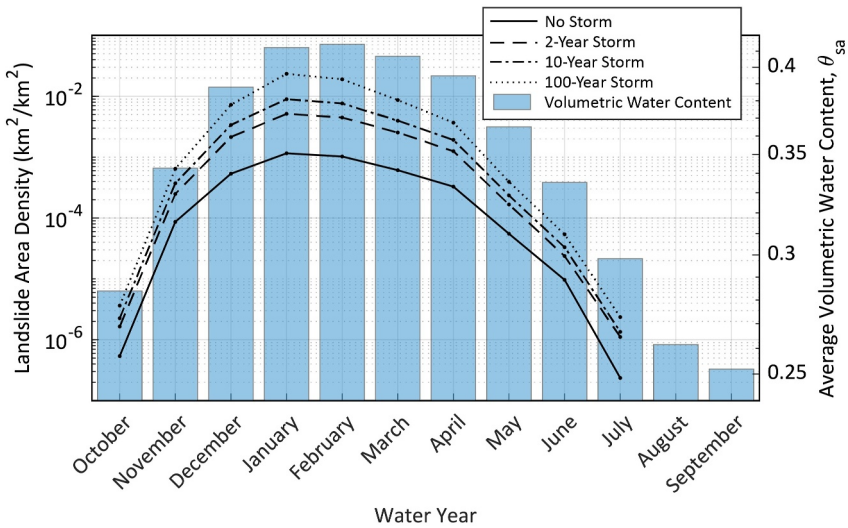

Figure 8. Landslide area density (LAD) for each month of the water year for antecedent moisture only (no event rainfall) and a range of event rainfall recurrence intervals of 2, 10 and 100 years.

conditions throughout the landscape, but capturing this would likely require assimilation with a landscape evolution model, which is beyond the scope of most slope stability approaches, including RG3D.

7.2. Relative Degree of Landsliding With Seasonality

To quantify variability in regional-scale landslide activity throughout the year, we compute landslide area density (LAD) for a range of event rainfall recurrence intervals applied during each month of the water year (a water year is the 12-month period 1 October through 30 September; Figure 8), where LAD is the total failed area normalized by the total area of the study area (1,068 km^2). The spatially averaged θ reflecting antecedent moisture for the study area, θ_{sa}, is shown for context. We assume $T = 80\%$, but this value may be adjusted to reflect uncertainty in soil shear strength or end-user preference and can be calibrated to match observed landslide distributions when available. LAD values represent individual scenarios (not cumulative landsliding throughout the year) and provide general insight into the relative influence of rainfall intensity on shallow landsliding over a wide range of antecedent moisture conditions. In the Pacific Northwest, landslides may occur on days with no recent rainfall due to the percolation and accumulation of antecedent rainfall within the subsurface, posing considerable challenges to landslide forecasting (e.g., Mirus, Becker, et al., 2018). To reflect this possibility, we model a baseline "No Storm" scenario highlighting the state of landslide susceptibility tied to seasonal antecedent rainfall with no event rainfall. These results may not reflect actual landslide activity for this precipitation scenario as some stabilizing processes are not included in this model (e.g., tree root reinforcement) but provide a useful comparison to the rainfall scenarios considered in this study.

Generally, LAD is highest in the wettest winter months (January and February) and negligible during the driest summer months (August and September), with LAD increasing rapidly from September to January and decreasing more gradually from February to August. This hysteretic behavior reflects changes in antecedent soil moisture as soils gradually dry out from spring to early fall and then wet up more rapidly as fall transitions into winter. Holding all other variables constant (month and antecedent moisture) and increasing event rainfall increases LAD for all months except for August and September, where landslide activity is negligible due to extremely dry soils. LAD increases more with event rainfall in wetter months compared to drier months, as less water is required to fill storage and satisfy field capacity, and more of the total rainfall may contribute to landslide triggering. There is little data to verify LAD values for this region and the modeled conditions, but historical LAD for Oregon is between 0% and 45%, depending on geological unit (Burns et al., 2016), and Radbruch-Hall et al. (1982) designated areal densities of <1.5%, 1.5%–15%, and >15% as low, medium, and high landslide incidences, respectively. Because wet months show the most change in LAD between event rainfall recurrence intervals, we focus on detailed evaluations of potential landsliding in February in the following sections.

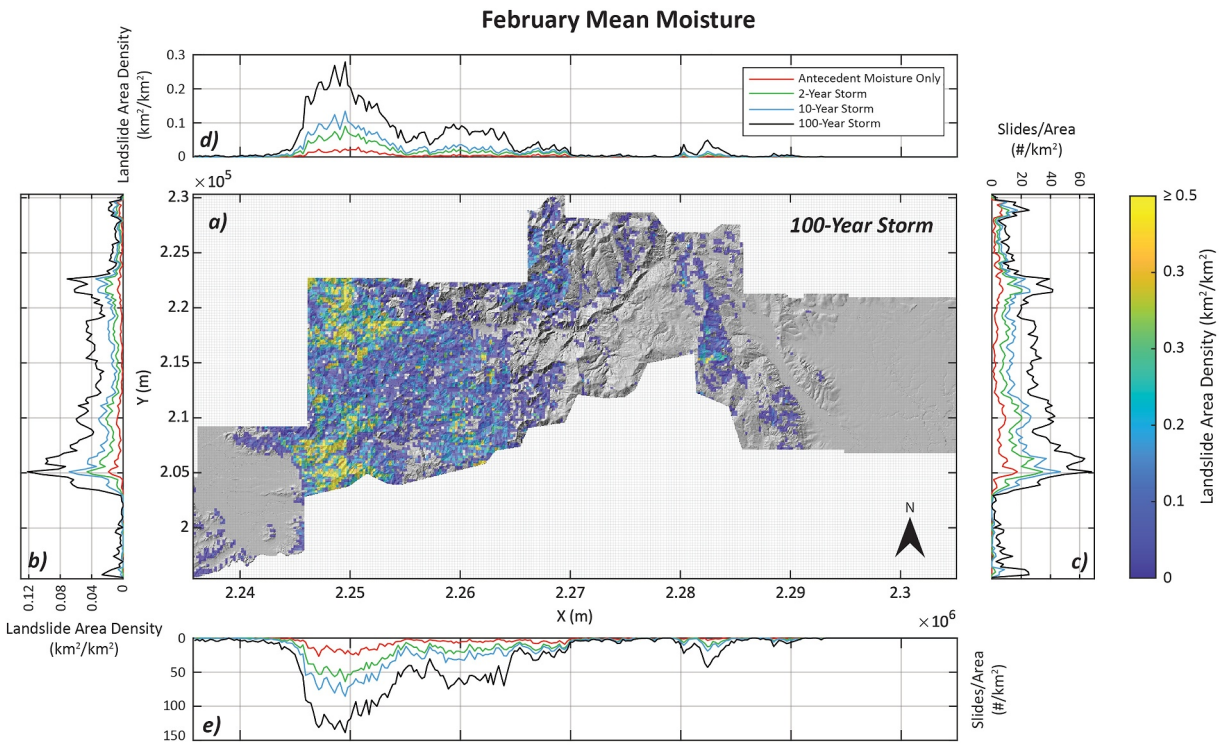

Figure 9. Landslide area density (LAD) and slides per area (S/A) for February mean antecedent moisture and a range of storm recurrence intervals: (a) LAD for 100-year storms; (b) LAD for each row; (c) S/A for each row; (d) LAD for each column; (e) S/A for each column. Hillshade was created using lidar provided by the Oregon Lidar Consortium (https://www.oregon.gov/dogami/lidar/pages/index.aspx).

7.3. Spatial Distribution of Landslide Density

We assess the spatial distribution of LAD and slides per area (S/A) for February mean antecedent moisture and a range of event rainfall recurrence intervals, where S/A is the number of landslides within a grid cell normalized by the grid cell area ($T = 50\%$; Figure 9). We compute S/A using a grid resolution of 240 m (0.058 km^2 per grid, or 1600 pixels of the original DEM raster) and assess LAD and S/A for the entire row of grid cells at each point on the *y*-axis (Figures 9b and 9c) and for the entire column of grid cells at each point on the *x*-axis (Figures 9d and 9e). We only evaluate areas in which digital elevation data are available.

High LAD and S/A are mainly concentrated in the western coastal mountains, especially in the south and north, and steadily decrease to the east where topography is less steep (Figure 9a). LAD and S/A are negligible both west of the coastal mountains and in the eastern half of the study area except for a pocket of moderate activity in the eastern coastal mountains west of the Gales Creek watershed (Figure 3). This region has exhibited historical landslide activity (Figure 3), but because RG3D is parameterized to assess shallow landslides and because the failure types of the inventoried landslides are largely unknown, we may miss them if governed by different failure mechanics (e.g., deep, rotational slides or debris flows).

The low levels of LAD and S/A for antecedent moisture only (no event rainfall) are primarily driven by topography, geomorphic properties (e.g., slope, soil depth), and the distribution of remotely sensed θ. LAD and S/A increase with event rainfall, with some regions increasing more than others due to heterogeneity of topography, geomorphic features, and antecedent moisture. Further, increases in LAD and S/A are spatially consistent with recurrence interval rainfall distributions (Figures 4b–4d), with the largest increases in LAD, S/A, and event rainfall occurring in the western half of the coastal mountains (Figures 9d and 9e). This spatial variability is not made immediately apparent through geomorphic scaling laws or single values of LAD.

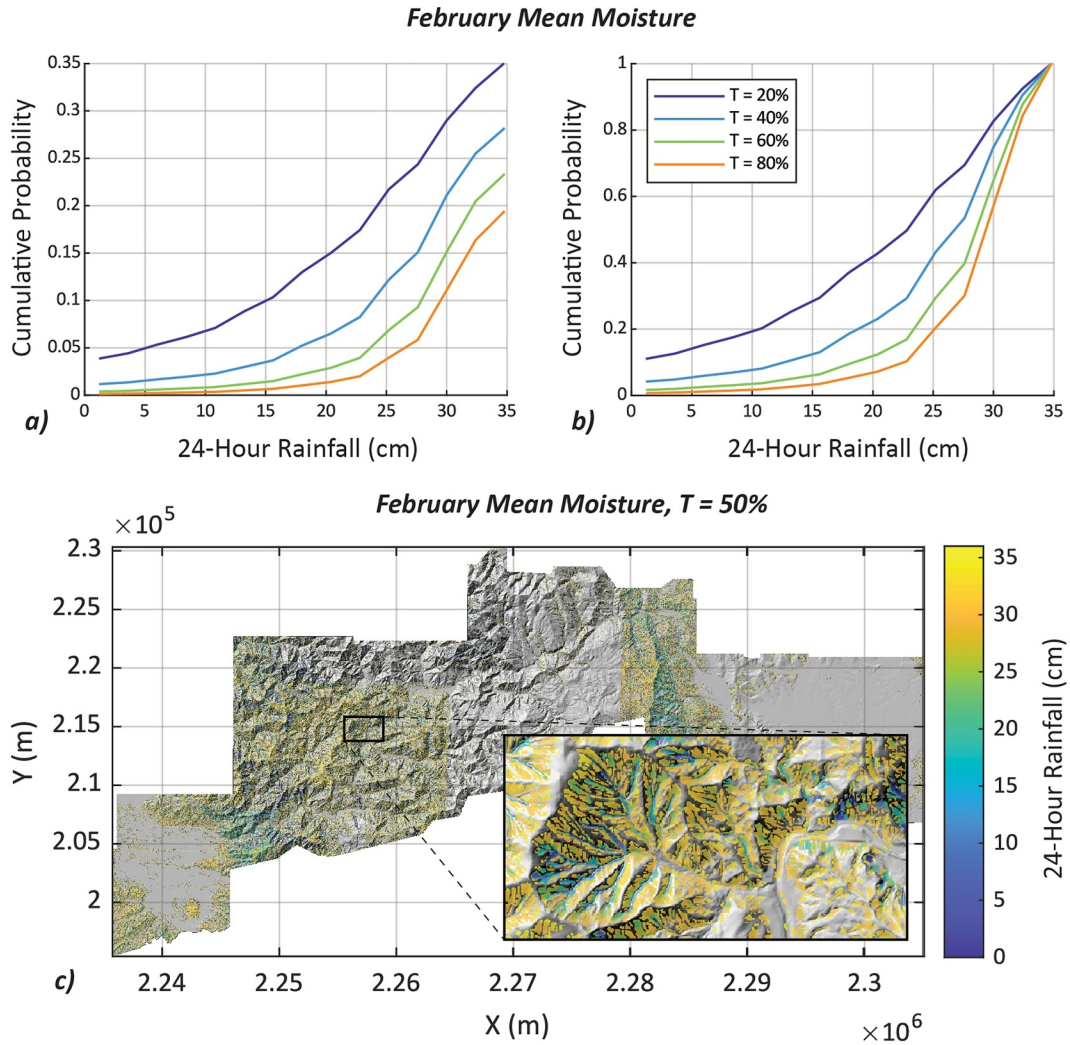

Figure 10. Rainfall threshold maps for February mean moisture: (a) cumulative distribution functions (CDFs) of rainfall thresholds (normalized by all columns); (b) CDFs of rainfall thresholds (normalized by failed columns only); and (c) map of rainfall thresholds for $T = 50\%$. $\boldsymbol{T}$ = threshold of susceptibility. Hillshade was created using lidar provided by the Oregon Lidar Consortium (https://www.oregon.gov/dogami/lidar/pages/index.aspx).

7.4. Rainfall Thresholds

We develop location-specific, susceptibility-based rainfall thresholds by (a) applying a series of uniform 24-hr rainfall rasters (e.g., 0 cm, 4 cm, 8 cm) and computing a susceptibility map for each one, (b) applying a susceptibility threshold to each map to create distributions of discrete landslides for each rainfall value, and (c) assigning the corresponding value of rainfall to each column superimposed by a landslide shape for each distribution of landslides. We repeat this process for a wide range of rainfall values (i.e., up to 36 cm in 24 hr) to create a map of rainfall thresholds where each column is assigned the lowest amount of rainfall required to cause landsliding, similar to q/T maps generated using SHALSTAB (Dietrich & Montgomery, 1998) or R/T maps generated using SINMAP (Pack et al., 1998).

Rainfall thresholds vary spatially with relatively low thresholds in the western coastal mountains and west of the Gales Creek watershed (Figure 10c; mean February antecedent moisture; $T = 50\%$). Thresholds are higher in the central region, possibly owing to the gentler hillslope architecture in this region, which reduces driving forces tied to soil weight and gravity, but also likely stemming from artifacts associated with the resolution of remotely sensed moisture data. The abrupt change in θ between 9-km SMAP cells is unrealistic, leading to unrealistic discontinuities in landsliding. Advances in methods of downscaling soil moisture data (e.g., Felsberg et al., 2021;

Grieco et al., 2018) may reduce the influence of such artifacts. Rainfall thresholds may vary within a small area and even upon the same hillslope, reflecting localized changes in slope angle and soil depth (inset in Figure 10c). This heterogeneity demonstrates the utility of maps as a supplement to binary rainfall thresholds typically used to characterize an entire region.

We summarize rainfall threshold maps using cumulative distribution functions (CDFs) of 24-hr event rainfall for a range of susceptibility thresholds, both normalized by the total number of columns in the study area (Figure 10a) and by the number of failed columns (only those assigned a rainfall threshold; Figure 10b). These CDFs, which show that thresholds increase with T, account for the likelihood of landsliding and uncertainties tied to landscape-scale mechanical and hydrological properties, as opposed to binary thresholds that simply define failure and no-failure conditions. For context, previously proposed 24-hr rainfall thresholds tied to four storms during 1996 and 1997 range from about 5 to >25 cm in this region (Wiley, 2000).

8. Comparison of Landslide Slope Angles and Volumes Between Physics-Based Models

The creation of geomorphic scaling relationships requires a distribution of discrete landslides. Existing studies that use physics-based models to produce scaling relationships typically use 1D LE methods (e.g., infinite slope with transient hydromechanical model) to assess the stability of individual grid cells and then group unstable cells based on proximity (Alvioli et al., 2014). This approach may underpredict landsliding potential in gentler terrain as it is heavily reliant on the slope angle of individual grid cells and does not account for realistic boundary forces associated with discrete landslides. RG3D predicts landslides in less steep terrain (Figure 11a) and of higher volume (Figure 11b) with region growing on (downslope soil is mobilized following incipient failure) than with region growing off (February mean moisture; 10-year storm; $T = 50\%$). With region growing off, RG3D closely resembles 1D LE models typically used to assess regional-scale slope stability, with the added consideration of landslide boundary forces. Other models that consider landslide growth during failure are typically used for smaller landscapes (Table 1) but may consider upslope growth (e.g., STEP-TRAMM; Lehmann & Or, 2012). For RG3D, including upslope growth increases landslide area more than volume due to soils typically being thinner near ridges (Text S1.1 in Supporting Information S1).

9. Assumptions and Limitations

To maintain numerical stability during region growth, we do not assess landslides composed of a single column (6 m × 6 m for our DEM), but shallow landslides of this size are not uncommon (Prancevic et al., 2020). Smaller landslides could be assessed through future improvements of the growth algorithm or use of a finer resolution DEM, but the latter would increase computational time for a DEM of equal area.

During region growth, we assume that unstable columns mobilize and entrain stable columns downslope and that all of these columns fail as a landslide. However, downslope columns could possibly stabilize an upslope instability, preventing a landslide altogether, or upslope columns could evacuate their failure surface instead of mobilizing columns below. We do not account for either of these processes, but the following condition could be implemented to account for landslide evacuation, potentially limiting downslope growth: if the passive resistance at the landslide toe exceeds the net driving force of the landslide, the landslide cluster evacuates its failure surface and the region growing ceases. Since all soil columns are initially evaluated for stability based on their basal shear resistance, we assume that any cells upslope of a cluster would remain stable despite any potential debuttressing. However, it is possible that upslope columns could be pulled downslope by tensile bonds such as tree roots (i.e., Lehmann & Or, 2012). We do not explicitly test this mechanism, but a study examining sensitivity to upslope growth is included in Text S1.1 in Supporting Information S1. Finally, we prioritize adding columns that best satisfy force equilibrium during growth to expedite and increase the likelihood of force closure, but more research would be valuable to determine the algorithms that most appropriately prioritize cell addition, such as that proposed by Bellugi, Milledge, Dietrich, McKean, et al. (2015). For example, prioritizing the addition of cells that provide the least stabilization may increase landslide size and encourage growth into steeper terrain.

We assume that the boundary soil structure of each landslide is defined using traditional earth pressure angles for cohesionless soil with a horizontal surface slope (Rankine, 1857; Section 2.2). We adopt this simplifying assumption because the forces exerted by the boundary soil structure are typically small compared to the forces exerted by the cluster main body (3%–4% for an example landslide shown in Text S1.6 in Supporting Information S1). Although we do account for surface slope angle by using the ground surface to define the upper extent

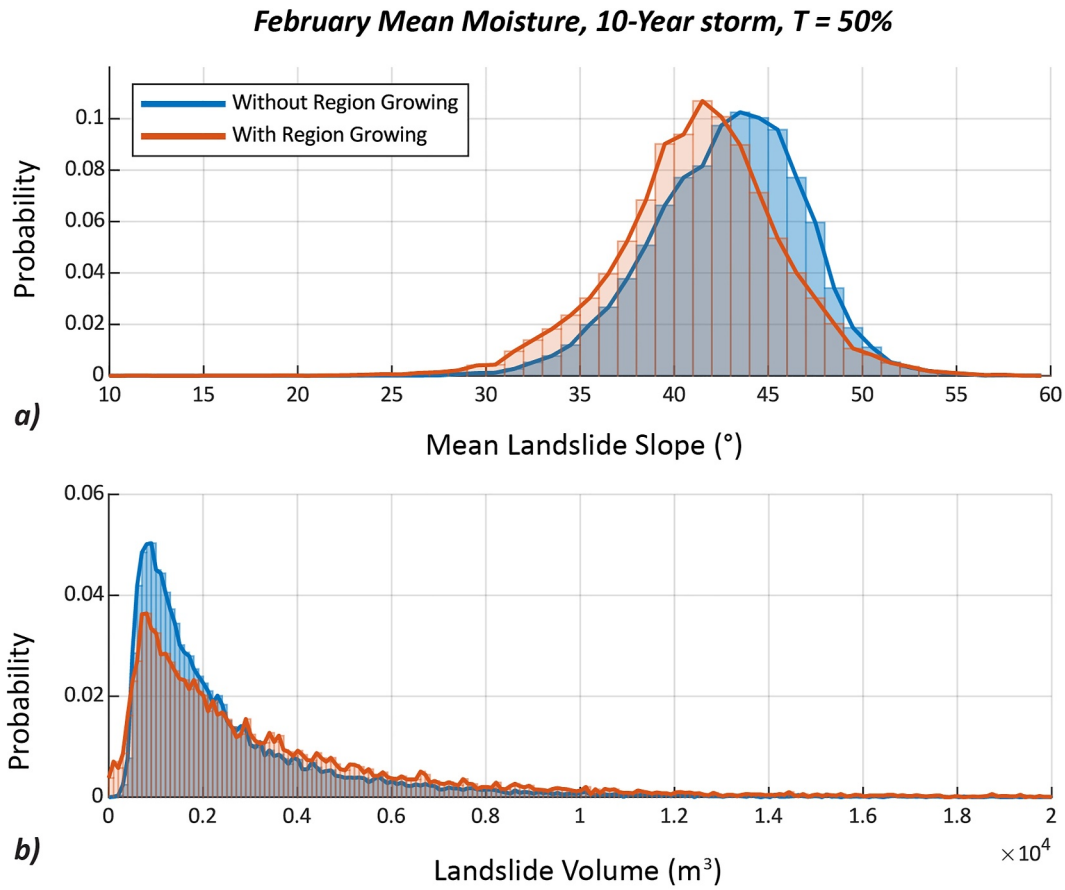

Figure 11. Comparison of RegionGrow3D-based landslides with and without region growing applied (February mean moisture; 10-year storm; T = 50%): (a) mean slope angle; and (b) volume. T = threshold of susceptibility.

of each boundary wedge (Figure 1d), alternative methods for determining earth pressure coefficients for soils with sloped surfaces and/or cohesion (Mazindrani & Ganjali, 1997) would likely improve estimates of forces tied to active and passive earth pressures at the landslide boundary (Milledge et al., 2014). Furthermore, depending on the geometry of a landslide and its direction of sliding, some prisms may generate passive earth pressure even if they are not at the toe of the landslide (e.g., a "T" shaped landslide projects prisms in the downslope direction at the bottom of the "upper arms"). As a simplifying assumption, we compute earth pressure angles depending on the orientation of the landslide boundary relative to the direction of sliding, but computing earth pressure angles using the orientation of the prism may further improve estimates of forces tied to earth pressures at the landslide boundary.

Forensic analysis of inventoried landslides is a valuable means of parameterizing RG3D and quantifying uncertainty in shear strength inputs; however, ideally, these landslides would be mechanistically similar to those modeled by RG3D. Like many inventories, SLIDO contains 2D geometry (planform), limited metadata, and a range of landslide types, while RG3D is solely focused on shallow, translational landslides. To best match RG3D, we forensically estimate the failure geometry for each SLIDO landslide and only back-calculate shear strength for landslides with mean depths between 1 and 5 m. However, this does not guarantee that all of these landslides are shallow, colluvial failures, and comparison of RG3D and SLIDO landslides shows differences in areas, mean depths, and volumes (Text S3 in Supporting Information S1). This reflects a limitation in the parametrization of RG3D that could be addressed by either (a) using an inventory specific to shallow landslides, which are limited in most regions, or (b) foregoing forensics and assuming a Gaussian—or otherwise—distribution of ϕ'. Despite these limitations, forensic back analysis provides an improved and physics-based means of estimating shear strength based on region-specific landslide characteristics.

We only consider vertical infiltration when quantifying the influence of event rainfall on suction stress and subsurface hydrology. This is a common assumption in the parameterization of some regional-scale slope stability models (e.g., TRIGRS) but does not reflect realistic gravity-driven water distribution that occurs during rainfall. Although modeling this type of subsurface hydrology is complex, relating soil wetness to topographic convergence (e.g., Dietrich et al., 1995; Pack et al., 1998) could be a simple and efficient means of partially addressing this limitation. In lieu of refined textural data at the scale of this analysis, we assume one soil texture and a set of van Genuchten parameters for each soil column; however, it is possible that these parameters could change with depth if a gradient of soil textures is present. Further, we do not consider root reinforcement or cohesion, but have provided sensitivity studies showing the potential influence of both on RG3D outputs (Text S1.4 and S1.5 in Supporting Information S1). We also assume homogenous soil interfacing with bedrock, acting as the failure surface for all landslides. The consideration of soil stratigraphy could be a substantial control on failure depth but would also increase computational time.

We used receiver operating characteristic (ROC) curves and the associated area under the curve (AUC) to compare results from RG3D to a landslide inventory (Section 6.1). This is a common method for evaluating models but carries unique challenges for regional-scale slope stability and landslide susceptibility models. First, landslide susceptibility models may identify potentially unstable terrain that has not yet failed, although it may have an appreciable likelihood of failure under certain conditions. Second, inventories are often incomplete and biased toward large deep-seated landslides, as shallow landslide scars are often smaller, have more subtle geomorphic signatures, and may be eroded and made obscure over shorter periods of time. Finally, there is a high level of uncertainty for regional-scale models, where precise parameterization is both cost-prohibitive and challenging. Thus, comparing RG3D outputs to inventories may result in high false positive rates that may not directly reflect the model's performance or utility. Further discussion related to this comparison and its limitations may be found in Text S3 in Supporting Information S1.

10. Conclusion

We present RG3D, a regional-scale, physics-based slope stability method and shallow landslide susceptibility framework based on the principles of 3D LE and the growth of discrete landslide geometries. We estimate uncertainty in regional-scale landsliding through 3D LE-based forensic analyses of inventoried landslides.

We use RG3D to evaluate geomorphic scaling relationships, seasonal and spatial trends in landslide initiation, and rainfall thresholds over a large region in the Oregon Coast Range (>1,000 km^2) considering: (a) the probability of failure, (b) heterogeneity in triggering conditions throughout a landscape, and (c) geomorphic and soil parameters. RG3D enables the creation of synthetic landslide distributions tied to triggers that have either not occurred or for which there are no high-quality landslide inventories available. These distributions include areas and volumes, which could help parameterize models tied to other mechanisms, such as debris flow initiation. We evaluate model performance using ROC curves and compare our results with published empirical relationships between landslide area, volume, and frequency. Using RG3D, we quantify the coupled influence of seasonal changes in antecedent soil moisture and event rainfall tied to a range of recurrence intervals on spatial trends in rainfall thresholds and landslide density that regional-scale empirical metrics may miss.

Data Availability Statement

The source code for RegionGrow3D is hosted in a repository at https://doi.org/10.5066/P1BSMGGD (Mathews & Leshchinsky, 2024). Basemap in Figures 3a and 3b provided by OpenStreetMap (OpenStreetMap contributors, 2017). Hillshade in Figure 1a, 2, 3b, 4b-d, 8a, and 9c created using lidar from the Oregon Lidar Consortium (Oregon Department of Geology and Mineral Industries, 2022). State boundary data in Figure 3a are provided by the U.S. Census Bureau (U.S. Census Bureau, 2011). Highway network data in Figure 3b were provided by the Oregon Department of Transportation (Oregon Department of Transportation, 2017). Soil texture data in Figure 3b were determined using sand and clay content data from SoilGrids250m (Hengl et al., 2017; https://files.isric.org/soilgrids/former/2017-03-10/data/). The landslide inventory extent in Figure 3b is from the Statewide Landslide Information Database for Oregon (SLIDO; Burns et al., 2012; Franczyk et al., 2019; https://www.oregon.gov/dogami/slido/Pages/data.aspx). Geological mapping data is from the Oregon Geological Data

Compilation (OGDC-7; Franczyk et al., 2020). Volumetric water content data in Figures 3c and 3d are from Soil Moisture Active Passive (SMAP; Reichle et al., 2019; accessed from https://appeears.earthdatacloud.nasa.gov/).

Acknowledgments
The authors gratefully acknowledge Dr. Josh Roering for providing the source code and guidance for the hillslope evolution model used in this study. We also thank the Oregon Department of Transportation (SPR 808) for funding the development of the RegionGrow3D model. Ben Leshchinsky and Michael Olsen acknowledge funding from the National Science Foundation under grant CMMI-2050047. Ben Leshchinsky acknowledges the support from USDA McIntire-Stennis project OREZ-FERM-898. Bill Schulz provided detailed and constructive comments on an earlier version of the RG3D model that helped greatly improve this work. Any use of trade, firm, or product names is for descriptive purposes only and does not imply endorsement by the U.S. Government.

References

Alberti, S., Leshchinsky, B., Roering, J., Perkins, J., & Olsen, M. J. (2022). Inversions of landslide strength as a proxy for subsurface weathering. *Nature Communications*, *13*(1), 6049. https://doi.org/10.1038/s41467-022-33798-5

Alvioli, M., & Baum, R. L. (2016). Parallelization of the TRIGRS model for rainfall-induced landslides using the message passing interface. *Environmental Modelling & Software*, *81*, 122–135. https://doi.org/10.1016/j.envsoft.2016.04.002

Alvioli, M., Guzzetti, F., & Rossi, M. (2014). Scaling properties of rainfall induced landslides predicted by a physically based model. *Geomorphology*, *213*, 38–47. https://doi.org/10.1016/j.geomorph.2013.12.039

Baum, R. L., & Godt, J. W. (2010). Early warning of rainfall-induced shallow landslides and debris flows in the USA. *Landslides*, *7*(3), 259–272. https://doi.org/10.1007/s10346-009-0177-0

Baum, R. L., Godt, J. W., & Savage, W. Z. (2010). Estimating the timing and location of shallow rainfall-induced landslides using a model for transient, unsaturated infiltration. *Journal of Geophysical Research*, *115*(F3), F03013. https://doi.org/10.1029/2009JF001321

Bellugi, D., Milledge, D. G., Dietrich, W. E., McKean, J. A., Perron, J. T., Sudderth, E. B., & Kazian, B. (2015). A spectral clustering search algorithm for predicting shallow landslide size and location: A shallow landslide search algorithm. *Journal of Geophysical Research: Earth Surface*, *120*(2), 300–324. https://doi.org/10.1002/2014JF003137

Bellugi, D., Milledge, D. G., Dietrich, W. E., Perron, J. T., & McKean, J. (2015). Predicting shallow landslide size and location across a natural landscape: Application of a spectral clustering search algorithm. *Journal of Geophysical Research: Earth Surface*, *120*(12), 2552–2585. https://doi.org/10.1002/2015JF003520

Bessette-Kirton, E. K., Cerovski-Darriau, C., Schulz, W. H., Coe, J. A., Kean, J. W., Godt, J. W., et al. (2019). Landslides triggered by Hurricane Maria: Assessment of an extreme event in Puerto Rico. *Geological Society of America Today*, *29*, 4–10. https://doi.org/10.1130/GSATG383A.1

Bogaard, T., & Greco, R. (2018). Invited perspectives: Hydrological perspectives on precipitation intensity-duration thresholds for landslide initiation: Proposing hydro-meteorological thresholds. *Natural Hazards and Earth System Sciences*, *18*(1), 31–39. https://doi.org/10.5194/nhess-18-31-2018

Bordoni, M., Meisina, C., Valentino, R., Lu, N., Bittelli, M., & Chersich, S. (2015). Hydrological factors affecting rainfall-induced shallow landslides: From the field monitoring to a simplified slope stability analysis. *Engineering Geology*, *193*, 19–37. https://doi.org/10.1016/j.enggeo.2015.04.006

Brien, D. L., & Reid, M. E. (2008). Assessing deep-seated landslide susceptibility using 3-D groundwater and slope-stability analyses, southwestern Seattle, Washington. In R. L. Baum, J. W. Godt, & L. M. Highland (Eds.), *Landslides and engineering geology of the Seattle, Washington, Area*. Geological Society of America. https://doi.org/10.1130/2008.4020(05)

Bunn, M., Leshchinsky, B., & Olsen, M. J. (2020a). Estimates of three-dimensional rupture surface geometry of deep-seated landslides using landslide inventories and high-resolution topographic data. *Geomorphology*, *367*, 107332. https://doi.org/10.1016/j.geomorph.2020.107332

Bunn, M., Leshchinsky, B., & Olsen, M. J. (2020b). Geologic trends in shear strength properties inferred through three-dimensional back analysis of landslide inventories. *Journal of Geophysical Research: Earth Surface*, *125*(9), e2019JF005461. https://doi.org/10.1029/2019JF005461

Burns, W., Duplantis, S., Mickelson, K., Spritzer, J., & Wells, R. (2012). *Landslide inventory maps of the Gales Creek quadrangle, Washington County, Oregon*. Oregon Department of Geology and Mineral Industries. Interpretive Map Series-46, Scale, 1, 8000.

Burns, W. J., Mickelson, K. A., & Madin, I. (2016). *Landslide susceptibility overview map of Oregon*. Oregon Department of Geology and Mineral Industries.

Caine, N. (1980). The Rainfall Intensity: Duration control of shallow landslides and debris flows. *Geografiska Annaler - Series A: Physical Geography*, *62*(1/2), 23–27. https://doi.org/10.2307/520449

Cohen, D., Schwarz, M., & Or, D. (2011). An analytical fiber bundle model for pullout mechanics of root bundles. *Journal of Geophysical Research*, *116*(F3), F03010. https://doi.org/10.1029/2010JF001886

De Vita, P., Napolitano, E., Godt, J. W., & Baum, R. L. (2013). Deterministic estimation of hydrological thresholds for shallow landslide initiation and slope stability models: Case study from the Somma-Vesuvius area of southern Italy. *Landslides*, *10*(6), 713–728. https://doi.org/10.1007/s10346-012-0348-2

Dietrich, W., & Montgomery, D. (1998). SHALSTAB: A digital terrain model for mapping shallow landslide potential. In *National council of the paper industry for air and stream improvement*. National Council of the Paper Industry for Air and Stream Improvement.

Dietrich, W. E., Reiss, R., Hsu, M.-L., & Montgomery, D. R. (1995). A process-based model for colluvial soil depth and shallow landsliding using digital elevation data. *Hydrological Processes*, *9*(3–4), 383–400. https://doi.org/10.1002/hyp.3360090311

Emberson, R., Kirschbaum, D. B., Amatya, P., Tanyas, H., & Marc, O. (2022). Insights from the topographic characteristics of a large global catalog of rainfall-induced landslide event inventories. *Natural Hazards and Earth System Sciences*, *22*(3), 1129–1149. https://doi.org/10.5194/nhess-22-1129-2022

Evans, T. M., & Baker, J. D. (2021). An effective stress framework for bearing capacity of shallow foundations in unsaturated soils. In *Presented at the proceedings of the 3rd international conference on sustainability in civil engineering* (pp. 3–14). Springer. https://doi.org/10.1007/978-981-16-0053-1_1

Felsberg, A., De Lannoy, G. J., Girotto, M., Poesen, J., Reichle, R. H., & Stanley, T. (2021). Global soil water estimates as landslide predictor: The effectiveness of SMOS, SMAP, and GRACE observations, land surface simulations, and data assimilation. *Journal of Hydrometeorology*, *22*(5), 1065–1084. https://doi.org/10.1175/JHM-D-20-0228.1

Franczyk, J. J., Burns, W. J., & Calhoun, N. C. (2019). Statewide Landslide Information Database for Oregon (SLIDO) - Release 4.0 [Dataset]. *Oregon*. https://www.oregon.gov/dogami/slido/Pages/data.aspx

Franczyk, J. J., Madin, I. P., Carlie, J. M. D., & McClaughry, J. D. (2020). Oregon Geologic Data Compilation (OGDC-7) [Dataset]. *Oregon Department of Geology and Mineral Industries (DOGAMI)*. https://pubs.oregon.gov/dogami/dds/p-OGDC-7.htm

Fusco, F., Mirus, B., Baum, R., Calcaterra, D., & De Vita, P. (2021). Incorporating the effects of complex soil layering and thickness local variability into distributed landslide susceptibility assessments. *Water*, *13*(5), 713. https://doi.org/10.3390/w13050713

Gao, L., Zhang, L. M., & Cheung, R. (2018). Relationships between natural terrain landslide magnitudes and triggering rainfall based on a large landslide inventory in Hong Kong. *Landslides*, *15*(4), 727–740. https://doi.org/10.1007/s10346-017-0904-x

Godt, J. W., Baum, R. L., Savage, W. Z., Salciarini, D., Schulz, W. H., & Harp, E. L. (2008). Transient deterministic shallow landslide modeling: Requirements for susceptibility and hazard assessments in a GIS framework. *Engineering Geology*, *102*(3–4), 214–226. https://doi.org/10.1016/j.enggeo.2008.03.019

Goldfinger, C., Nelson, C., Morey, A., Johnson, J., Patton, J., Karabanov, E., et al. (2012). Turbidite event history—Methods and implications for Holocene paleoseismicity of the Cascadia subduction zone. *USGS Professional Paper, 1661-F* (pp. 184). https://doi.org/10.3133/pp1661F

Grieco, N. R., Niemann, J. D., Green, T. R., Jones, A. S., & Grazaitis, P. J. (2018). Hydrologic downscaling of soil moisture using global data sets without site-specific calibration. *Journal of Hydrologic Engineering*, *23*(11), 04018048. https://doi.org/10.1061/(ASCE)HE.1943-5584.0001702

Guzzetti, F., Ardizzone, F., Cardinali, M., Rossi, M., & Valigi, D. (2009). Landslide volumes and landslide mobilization rates in Umbria, central Italy. *Earth and Planetary Science Letters*, *279*(3–4), 222–229. https://doi.org/10.1016/j.epsl.2009.01.005

Guzzetti, F., Mondini, A. C., Cardinali, M., Fiorucci, F., Santangelo, M., & Chang, K.-T. (2012). Landslide inventory maps: New tools for an old problem. *Earth-Science Reviews*, *112*(1–2), 42–66. https://doi.org/10.1016/j.earscirev.2012.02.001

Guzzetti, F., Peruccacci, S., Rossi, M., & Stark, C. P. (2007). Rainfall thresholds for the initiation of landslides in central and southern Europe. *Meteorology and Atmospheric Physics*, *98*(3), 239–267. https://doi.org/10.1007/s00703-007-0262-7

He, J., Qiu, H., Qu, F., Hu, S., Yang, D., Shen, Y., et al. (2021). Prediction of spatiotemporal stability and rainfall threshold of shallow landslides using the TRIGRS and Scoops3D models. *Catena*, *197*, 104999. https://doi.org/10.1016/j.catena.2020.104999

Hengl, T., Mendes de Jesus, J., Heuvelink, G. B. M., Ruiperez Gonzalez, M., Kilibarda, M., Blagotić, A., et al. (2017). SoilGrids250m: Global gridded soil information based on machine learning. *PLOS ONE*, *12*(2), e0169748. https://doi.org/10.1371/journal.pone.0169748

Hess, D. M., Leshchinsky, B. A., Bunn, M., Benjamin Mason, H., & Olsen, M. J. (2017). A simplified three-dimensional shallow landslide susceptibility framework considering topography and seismicity. *Landslides*, *14*(5), 1677–1697. https://doi.org/10.1007/s10346-017-0810-2

Highland, L., & Bobrowsky, P. T. (2008). *The landslide handbook: A guide to understanding landslides*. U.S. Geological Survey Circular 1324. https://doi.org/10.3133/CIR1325

Hosmer, D. W., & Lemeshow, S. (1989). *Applied logistic regression*. Wiley. Retrieved from https://books.google.com/books?id=-p5qAAAAMAAJ

Hovland, H. J. (1977). Three-dimensional slope stability analysis method. *Journal of the Geotechnical Engineering Division*, *103*(9), 971–986. https://doi.org/10.1061/AJGEB6.0000493

Keefer, D. K., Wilson, R. C., Mark, R. K., Brabb, E. E., Brown, W. M., III, Ellen, S. D., et al. (1987). Real-time landslide warning during heavy rainfall. *Science*, *238*(4829), 921–925. https://doi.org/10.1126/science.238.4829.921

LaHusen, S. R., Duvall, A. R., Booth, A. M., Grant, A., Mishkin, B. A., Montgomery, D. R., et al. (2020). Rainfall triggers more deep-seated landslides than Cascadia earthquakes in the Oregon Coast Range, USA. *Science Advances*, *6*(38), eaba6790. https://doi.org/10.1126/sciadv.aba6790

Lee, S. (2005). Application of logistic regression model and its validation for landslide susceptibility mapping using GIS and remote sensing data. *International Journal of Remote Sensing*, *26*(7), 1477–1491. https://doi.org/10.1080/01431160412331331012

Lee, S., & Talib, J. A. (2005). Probabilistic landslide susceptibility and factor effect analysis. *Environmental Geology*, *47*(7), 982–990. https://doi.org/10.1007/s00254-005-1228-z

Lehmann, P., & Or, D. (2012). Hydromechanical triggering of landslides: From progressive local failures to mass release. *Water Resources Research*, *48*(3), W03535. https://doi.org/10.1029/2011WR010947

Lehmann, P., von Ruette, J., & Or, D. (2019). Deforestation effects on rainfall-induced shallow landslides: Remote sensing and physically-based modelling. *Water Resources Research*, *55*(11), 9962–9976. https://doi.org/10.1029/2019WR025233

Leshchinsky, B., Lehmann, P., & Or, D. (2021). Enhanced rainfall-induced shallow landslide activity following seismic disturbance—From triggering to healing. *Journal of Geophysical Research: Earth Surface*, *126*(1). https://doi.org/10.1029/2020JF005669

Lu, N., & Godt, J. (2008). Infinite slope stability under steady unsaturated seepage conditions. *Water Resources Research*, *44*(11), W11404. https://doi.org/10.1029/2008WR006976

Malamud, B. D., Turcotte, D. L., Guzzetti, F., & Reichenbach, P. (2004). Landslide inventories and their statistical properties. *Earth Surface Processes and Landforms*, *29*(6), 687–711. https://doi.org/10.1002/esp.1064

Marin, R. J. (2020). Physically based and distributed rainfall intensity and duration thresholds for shallow landslides. *Landslides*, *17*(12), 2907–2917. https://doi.org/10.1007/s10346-020-01481-9

Martin, Y., Rood, K., Schwab, J. W., & Church, M. (2002). Sediment transfer by shallow landsliding in the Queen Charlotte Islands, British Columbia. *Canadian Journal of Earth Sciences*, *39*(2), 189–205. https://doi.org/10.1139/e01-068

Mathews, N. W., & Leshchinsky, B. A. (2024). RegionGrow3D: A software for characterizing discrete three-dimensional landslide source areas on a regional scale (version 1.0.0) [Software]. *U.S. Geological Survey Software Release*. https://doi.org/10.5066/P1BSMGGD

Mazindrani, Z., & Ganjali, M. (1997). Lateral earth pressure problem of cohesive backfill with inclined surface. *Journal of Geotechnical and Geoenvironmental Engineering*, *123*(2), 110–112. https://doi.org/10.1061/(ASCE)1090-0241(1997)123:2(110)

Medwedeff, W. G., Clark, M. K., Zekkos, D., & West, A. J. (2020). Characteristic landslide distributions: An investigation of landscape controls on landslide size. *Earth and Planetary Science Letters*, *539*, 116203. https://doi.org/10.1016/j.epsl.2020.116203

Mergili, M., Marchesini, I., Rossi, M., Guzzetti, F., & Fellin, W. (2014). Spatially distributed three-dimensional slope stability modelling in a raster GIS. *Geomorphology*, *206*, 178–195. https://doi.org/10.1016/j.geomorph.2013.10.008

Milledge, D. G., Bellugi, D., McKean, J. A., Densmore, A. L., & Dietrich, W. E. (2014). A multidimensional stability model for predicting shallow landslide size and shape across landscapes: Predicting landslide size and shape. *Journal of Geophysical Research: Earth Surface*, *119*(11), 2481–2504. https://doi.org/10.1002/2014JF003135

Mirus, B. B., Morphew, M., & Smith, J. (2018). Developing hydro-meteorological thresholds for shallow landslide initiation and early warning. *Water*, *10*(9), 1274. https://doi.org/10.3390/w10091274

Mirus, B. B., Becker, R. E., Baum, R. L., & Smith, J. B. (2018). Integrating real-time subsurface hydrologic monitoring with empirical rainfall thresholds to improve landslide early warning. *Landslides*, *15*(10), 1909–1919. https://doi.org/10.1007/s10346-018-0995-z

Mirus, B. B., Ebel, B. A., Loague, K., & Wemple, B. C. (2007). Simulated effect of a forest road on near-surface hydrologic response: Redux. *Earth Surface Processes and Landforms: The Journal of the British Geomorphological Research Group*, *32*(1), 126–142. https://doi.org/10.1002/esp.1387

Montgomery, D. R., & Dietrich, W. E. (1994). A physically based model for the topographic control on shallow landsliding. *Water Resources Research*, *30*(4), 1153–1171. https://doi.org/10.1029/93WR02979

Napolitano, E., Fusco, F., Baum, R. L., Godt, J. W., & De Vita, P. (2016). Effect of antecedent-hydrological conditions on rainfall triggering of debris flows in ash-fall pyroclastic mantled slopes of Campania (southern Italy). *Landslides*, *13*(5), 967–983. https://doi.org/10.1007/s10346-015-0647-5

Okimura, T., & Ichikawa, R. (1985). A prediction method for surface failures by movements of infiltrated water in a surface soil layer. *Natural Disaster Science*, *7*(1), 41–51.
OpenStreetMap contributors. (2017). OpenStreetMap Basemap [Dataset]. *OpenStreetMap*. Retrieved from https://www.openstreetmap.org
Oregon Department of Geology and Mineral Industries. (2022). Oregon lidar consortium [Dataset]. *Oregon*. Retrieved from https://www.oregon.gov/dogami/lidar/Pages/index.aspx
Oregon Department of Transportation. (2014). Hydraulics design manual. *Highway Division*.
Oregon Department of Transportation. (2017). Highway network [Dataset]. *Oregon*. Retrieved from https://www.oregon.gov/odot/Data/Pages/GIS-Data.aspx
Pack, R. T., Tarboton, D. G., & Goodwin, C. N. (1998). The SINMAP approach to terrain stability mapping. In *Proceedings of the 8th congress of the international association of engineering geology, Vancouver, British Columbia* (pp. 21–25). Canada.
Patton, A. I., Luna, L. V., Roering, J. J., Jacobs, A., Korup, O., & Mirus, B. B. (2023). Landslide initiation thresholds in data-sparse regions: Application to landslide early warning criteria in Sitka, Alaska, USA. *Natural Hazards and Earth System Sciences*, *23*(10), 3261–3284. https://doi.org/10.5194/nhess-23-3261-2023
Perkins, J. P., Reid, M. E., & Schmidt, K. M. (2017). Control of landslide volume and hazard by glacial stratigraphic architecture, northwest Washington State, USA. *Geology*, *45*(12), 1139–1142. https://doi.org/10.1130/G39691.1
Peterson, C. D., Minor, R., Peterson, G. L., & Gates, E. B. (2011). Pre-and post-Missoula flood geomorphology of the pre-Holocene ancestral Columbia River Valley in the Portland forearc basin, Oregon and Washington, USA. *Geomorphology*, *129*(3), 276–293. https://doi.org/10.1016/j.geomorph.2011.02.022
Pourghasemi, H. R., Teimoori Yansari, Z., Panagos, P., & Pradhan, B. (2018). Analysis and evaluation of landslide susceptibility: A review on articles published during 2005–2016 (periods of 2005–2012 and 2013–2016). *Arabian Journal of Geosciences*, *11*(9), 193. https://doi.org/10.1007/s12517-018-3531-5
Prancevic, J. P., Lamb, M. P., McArdell, B. W., Rickli, C., & Kirchner, J. W. (2020). Decreasing landslide erosion on steeper slopes in soil-mantled landscapes. *Geophysical Research Letters*, *47*(10), e2020GL087505. https://doi.org/10.1029/2020GL087505
Radbruch-Hall, D. H., Colton, R. B., Davies, W. E., Lucchitta, I., Skipp, B. A., & Varnes, D. J. (1982). *Landslide overview map of the conterminous United States (No. 2330–7102)*. US Geological Survey. https://doi.org/10.3133/pp1183
Rankine, W. J. M. (1857). II. On the stability of loose earth. *Philosophical Transactions of the Royal Society of London*, *147*, 9–27. https://doi.org/10.1098/rstl.1857.0003
Reichenbach, P., Rossi, M., Malamud, B. D., Mihir, M., & Guzzetti, F. (2018). A review of statistically-based landslide susceptibility models. *Earth-Science Reviews*, *180*, 60–91. https://doi.org/10.1016/j.earscirev.2018.03.001
Reichle, R. H., De Lannoy, G. J. M., Liu, Q., Ardizzone, J. V., Colliander, A., Conaty, A., et al. (2017). Assessment of the SMAP Level-4 surface and root-zone soil moisture product using in situ measurements. *Journal of Hydrometeorology*, *18*(10), 2621–2645. https://doi.org/10.1175/JHM-D-17-0063.1
Reichle, R. H., Liu, Q., Koster, R. D., Crow, W. T., De Lannoy, G. J. M., Kimball, J. S., et al. (2019). Version 4 of the SMAP Level-4 soil moisture algorithm and data product [Dataset]. *Journal of Advances in Modeling Earth Systems*, *11*(10), 3106–3130. https://doi.org/10.1029/2019MS001729
Reid, M. E., Christian, S. B., Brien, D. L., & Henderson, S. T. (2015). *Scoops3D: Software to analyze 3D slope stability throughout a digital landscape* (p. 236). U.S. Geological Survey Techniques and Methods 14-A1. https://doi.org/10.3133/tm14A1
Roering, J. J. (2008). How well can hillslope evolution models "explain" topography? Simulating soil transport and production with high-resolution topographic data. *Geological Society of America Bulletin*, *120*(9–10), 1248–1262. https://doi.org/10.1130/B26283.1
Schaap, M. G., Leij, F. J., & van Genuchten, M. T. (2001). ROSETTA: A computer program for estimating soil hydraulic parameters with hierarchical pedotransfer functions. *Journal of Hydrology*, *251*(3–4), 163–176. https://doi.org/10.1016/S0022-1694(01)00466-8
Schmidt, K., Roering, J., Stock, J., Dietrich, W., Montgomery, D., & Schaub, T. (2001). The variability of root cohesion as an influence on shallow landslide susceptibility in the Oregon Coast Range. *Canadian Geotechnical Journal*, *38*(5), 995–1024. https://doi.org/10.1139/t01-031
Schwanghart, W., & Scherler, D. (2014). Short communication: TopoToolbox 2 – MATLAB-based software for topographic analysis and modeling in Earth surface sciences. *Earth Surface Dynamics*, *2*(1), 1–7. https://doi.org/10.5194/esurf-2-1-2014
Schwarz, M., Cohen, D., & Or, D. (2010). Root-soil mechanical interactions during pullout and failure of root bundles. *Journal of Geophysical Research*, *115*(F4), F04035. https://doi.org/10.1029/2009JF001603
Segoni, S., Piciullo, L., & Gariano, S. L. (2018). A review of the recent literature on rainfall thresholds for landslide occurrence. *Landslides*, *15*(8), 1483–1501. https://doi.org/10.1007/s10346-018-0966-4
Serey, A., Piñero-Feliciangeli, L., Sepúlveda, S. A., Poblete, F., Petley, D. N., & Murphy, W. (2019). Landslides induced by the 2010 Chile megathrust earthquake: A comprehensive inventory and correlations with geological and seismic factors. *Landslides*, *16*(6), 1153–1165. https://doi.org/10.1007/s10346-019-01150-6
Smith, R., & Roe, W. (2015). *Oregon geologic data compilation (OGDC)—Release 6*. Oregon Department of Geology and Mineral Industries (DOGAMI). Open-File Rept. O-13, 12.
Soil Survey Staff. (1975). Soil taxonomy: A basic system of soil classification of making and interpreting soil surveys. In *Natural resources conservation service. U.S. Department of Agriculture Handbook no. 436*. USDA-SCS.
Tanyaş, H., Westen, C. J., Allstadt, K. E., & Jibson, R. W. (2019). Factors controlling landslide frequency–area distributions. *Earth Surface Processes and Landforms*, *44*(4), 900–917. https://doi.org/10.1002/esp.4543
Taylor, D. W. (1948). Fundamentals of soil mechanics. *Soil Science*, *66*(2), 161. https://doi.org/10.1097/00010694-194808000-00008
Terzaghi, K. (1950). Mechanism of landslides. In S. Paige (Ed.), *Application of geology to engineering practice* (p. 0). Geological Society of America. https://doi.org/10.1130/Berkey.1950.83
Terzaghi, K., Peck, R. B., & Mesri, G. (1996). *Soil mechanics in engineering practice*. John Wiley & Sons.
Thomas, M. A., Collins, B. D., & Mirus, B. B. (2019). Assessing the feasibility of satellite-based thresholds for hydrologically driven landsliding. *Water Resources Research*, *55*(11), 9006–9023. https://doi.org/10.1029/2019WR025577
Thomas, M. A., Mirus, B. B., & Collins, B. D. (2018). Identifying physics-based thresholds for rainfall-induced landsliding. *Geophysical Research Letters*, *45*(18), 9651–9661. https://doi.org/10.1029/2018GL079662
U.S. Census Bureau. (2011). State boundaries (generalized for Mapping) [Dataset]. *ScienceBase*. Retrieved from https://www.sciencebase.gov/catalog/item/52c78623e4b060b9ebca5be5
Valenzuela, P., Domínguez-Cuesta, M. J., Mora García, M. A., & Jiménez-Sánchez, M. (2018). Rainfall thresholds for the triggering of landslides considering previous soil moisture conditions (Asturias, NW Spain). *Landslides*, *15*(2), 273–282. https://doi.org/10.1007/s10346-017-0878-8
van Genuchten, M. T. (1980). A closed-form equation for predicting the hydraulic conductivity of unsaturated soils. *Soil Science Society of America Journal*, *44*(5), 892–898. https://doi.org/10.2136/sssaj1980.03615995004400050002x

van Westen, C. J., Castellanos, E., & Kuriakose, S. L. (2008). Spatial data for landslide susceptibility, hazard, and vulnerability assessment: An overview. *Engineering Geology*, *102*(3–4), 112–131. https://doi.org/10.1016/j.enggeo.2008.03.010

Wartman, J., Dunham, L., Tiwari, B., & Pradel, D. (2013). Landslides in Eastern Honshu Induced by the 2011 Tohoku Earthquake. *Bulletin of the Seismological Society of America*, *103*(2B), 1503–1521. https://doi.org/10.1785/0120120128

Wieczorek, G. F. (1996). Landslides: Investigation and mitigation. In *Chapter 4-Landslide triggering mechanisms. Transportation research board special report* (p. 247).

Wiley, T. (2000). Relationship between rainfall and debris flows in western Oregon. *Oregon Geology*, *62*(2), 27–43.

Zhang, S., & Wang, F. (2019). Three-dimensional seismic slope stability assessment with the application of Scoops3D and GIS: A case study in Atsuma, Hokkaido. *Geoenvironmental Disasters*, *6*(1), 9. https://doi.org/10.1186/s40677-019-0125-9

Zhang, S. J., Xu, C. X., Wei, F. Q., Hu, K. H., Xu, H., Zhao, L. Q., & Zhang, G. P. (2020). A physics-based model to derive rainfall intensity-duration threshold for debris flow. *Geomorphology*, *351*, 106930. https://doi.org/10.1016/j.geomorph.2019.106930

References From the Supporting Information

Chiang, S.-H., & Chang, K.-T. (2011). The potential impact of climate change on typhoon-triggered landslides in Taiwan, 2010–2099. *Geomorphology*, *133*(3–4), 143–151. https://doi.org/10.1016/j.geomorph.2010.12.028

Culmann, K. (1864). *Die graphische Statik*. Meyer und Zeller. Retrieved from https://books.google.com/books?id=-HiztAEACAAJ

Lu, N., & Likos, W. J. (2006). Suction stress characteristic curve for unsaturated soil. *Journal of Geotechnical and Geoenvironmental Engineering*, *132*(2), 131–142. https://doi.org/10.1061/(ASCE)1090-0241(2006)132:2(131)

Lu, N., & Likos, W. J. (2013). Origin of cohesion and its dependence on saturation for granular media. In *Poromechanics V* (pp. 1669–1675). American Society of Civil Engineers. https://doi.org/10.1061/9780784412992.197

Marc, O., Stumpf, A., Malet, J.-P., Gosset, M., Uchida, T., & Chiang, S.-H. (2018). Initial insights from a global database of rainfall-induced landslide inventories: The weak influence of slope and strong influence of total storm rainfall. *Earth Surface Dynamics*, *6*(4), 903–922. https://doi.org/10.5194/esurf-6-903-2018

Quenzer, R., & Friesz, A. M. (2015). *AppEEARS: Simple and intuitive access to analysis ready data* (Vol. 2015, p. IN51B-1801). Presented at the AGU Fall Meeting Abstracts.

Stanley, T., & Kirschbaum, D. B. (2017). A heuristic approach to global landslide susceptibility mapping. *Natural Hazards*, *87*(1), 145–164. https://doi.org/10.1007/s11069-017-2757-y

Wu, T. H., McKinnell III, W. P., & Swanston, D. N. (1979). Strength of tree roots and landslides on Prince of Wales Island, Alaska. *Canadian Geotechnical Journal*, *16*(1), 19–33. https://doi.org/10.1139/t79-003